

SEL-63-011

CATALOGED BY
ACTIA
402964

Some Backscatter, Sweep-Frequency Observations

402 964

by

S. N. Denno* and O. G. Villard, Jr.

February 1963

Technical Report No. 72

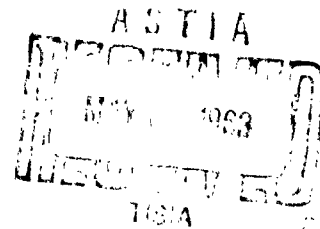
Prepared under

Office of Naval Research Contract

Nonr-225(64), NR 088-003, and

Advanced Research Projects Agency ARPA Order 196-62

* Supported by National Research Council Fellowship
National Academy of Sciences



RADIOSCIENCE LABORATORY

STANFORD ELECTRONICS LABORATORIES

STANFORD UNIVERSITY • STANFORD, CALIFORNIA



ASTIA AVAILABILITY NOTICE

Qualified requesters may obtain copies of this report from ASTIA. Foreign announcement and dissemination of this report by ASTIA is limited.

February 1963

ERRATA

<u>Page</u>	<u>Location</u>	<u>Should Read</u>
vi	Line 3 from bottom	at the assumed position of the irregularity ...53
6	Line 3 from bottom	$ 1/(dP'/d\beta_0) $. It is obvious that...
11	Line 5 below Eq. (16)	path. This function provides a rough approximation...
	Line 2 below Eq. (17)	with this angle and occurs at an additional normalized height of
14	Line 6 below Eq. (19)	transmitter, viz., 0° , $+30^\circ$, $+60^\circ$, and -60° for b equal to...
24	Line 8 from bottom	...of distance traveled by each ray on echo intensity, the num-
30	Line 12 from bottom	...in the region of maximum frequency, no longer bears...
33	Fig. 21 A-1 above top strip	22 June 1962
45	Line 4	frequency range of 15 - 24 Mc/s, show, on the...
53	Last line of legend	ASSUMED POSITION OF THE IRREGULARITY.
63	Eq. (D.3)	$\overline{BC} = \overline{PC} \cos \beta$.
	Eq. (D.6)	$\dots \sin^2 \beta = -2 \overline{PA} \cdot \overline{PC} \cos \alpha \dots$

SEL-63-011

SOME BACKSCATTER, SWEEP-FREQUENCY OBSERVATIONS

by

S. N. Denno* and O. G. Villard, Jr.

February 1963

Reproduction in whole or in part
is permitted for and purpose of
the United States Government.

Technical Report No. 72

Prepared under
Office of Naval Research Contract
Nonr-225(64), NR 088-003, and
Advanced Research Projects Agency ARPA Order 196-62

*Supported by
National Research Council Fellowship
National Academy of Sciences

Radioscience Laboratory
Stanford Electronics Laboratories
Stanford University Stanford, California

ABSTRACT

Analysis of the sweep-frequency, ground-backscatter echo is attempted by the application of ray theory. The variation of the time delay of the various portions of the radar echo is studied through two different methods: 1) calculation of the equivalent group path, and 2) tracing the actual group path by means of an analog computer. Special attention is given the two limiting rays--the tangent ray and the minimum-time-delay ray--in the study of their behavior with frequency, since they determine the shape of the sweep-frequency pattern. Both approaches agree well with experimental observations. The effects of the layer parameters on the shape are briefly investigated; these include the layer model, its thickness, and the presence of horizontal gradients.

A study of the striations that appear within the Sweep-Frequency Echo (SFE) is also reported. A description is given of continuous soundings made over a limited period in the summer of 1962 in the eastward and westward directions from Stanford, California, for the purpose of determining their time and frequency characteristics. Two distinct types are separated according to the variation of their time delay with frequency. With the aid of the above analysis, it is shown that the frequency-dependent striations may be caused by layer stratification or by the presence of not too intense electron-density "blobs" embedded in the F-layer, while those that are frequency-independent are the result of highly reflective irregularities in the propagation path. The location of these irregularities is, so far, a matter of speculation, but it is thought that the E-layer is a quite possible one, and that some of these irregularities may be identified with ordinary sporadic E and also with the middle-latitude variety of field-aligned irregularities. The geometrical conditions are explored under which the latter kind may be illuminated by an F-layer-propagated ray in the downward part of its path while satisfying normal incidence with their long axis. Further work is recommended to pin down the location of these irregularities and to extend knowledge of their characteristics.

CONTENTS

Chapter	Page
I. INTRODUCTION	1
II. CHARACTERISTICS OF THE BACKSCATTER ECHO	2
A. The Reflected Echo and Its Presentation	2
B. Group Path and Time Delay	2
C. The Equivalent Path Approach	5
D. The Ray-Tracing Approach	7
1. General	7
2. Ray Tracings with a β -Chapman Layer	9
3. Derivation of Time Delay and Its Relation to the Backscatter Echo	24
E. Analysis of Factors Affecting Shape of Backscatter Echo	30
III. SOUNDING EXPERIMENTS	42
IV. DISCUSSION OF DATA	45
A. General	45
B. Constant-Range Echoes	47
1. General	47
2. Ground Objects and F-Layer Irregularities	47
3. Irregularities in the E Layer	50
V. CONCLUSIONS AND RECOMMENDATIONS	54
 APPENDIX	
A. Derivation of the Equivalent Group Path as a Function of the Take-Off Angle for Curved Geometry	56
1. In Terms of Virtual Height	56
2. In Terms of Layer Parameters	57
3. Rate of Variation	58
B. Geometry of Transmission Path with Respect to Sun's Zenith Angle	59
C. Derivation of Echo Group Time Delay	60
D. Determination of the Angle of the Downcoming Ray Meeting a Geomagnetic Field Line at Right Angles	62
REFERENCES	64

TABLES

Number	Page
1. Examples of Limit Echoes	46

ILLUSTRATIONS

Figure	Page
1. Geometry of equivalent ray path	3
2. Graphical construction showing the variation of the equivalent group path P' of a ray with the elevation angle β_0 at different normalized frequencies ρ	6
3. Equivalent path P' and height h' at elevation angles β_0 and normalized frequencies of 1.0, 1.5, 2.0, and 2.5, for a parabolic F layer of $h_0 = 200$ km and $y_m = 100$ km.	8
4. Shape of sweep-frequency, ground-backscattered echo, bounded by its two extreme time delays as functions of the normalized frequency. Parabolic layer of $h_0 = 200$ km, $y_m = 100$ km	9
5. Tracings of rays of various take-off angles in a β -Chapman layer. $S(x) = 1$	12
6. Tracings of rays of various take-off angles in a β -Chapman layer. $S(x) = \cos [(x-b)/R]$; $b = 0$ km	16
7. Tracings of rays of various take-off angles in a β -Chapman layer. $S(x) = \cos [(x-b)/R]$; $b = 3333$ km	18
8. Tracings of rays of various take-off angles in a β -Chapman layer. $S(x) = \cos [(x-b)/R]$; $b = 6667$ km	20
9. Tracings of rays of various take-off angles in a β -Chapman layer at 1-deg intervals. $S(x) = \cos [(x-b)/R]$; $b = -6667$ km	22
10. Variation of pulse time delay T with take-off angle β_0 at various values of normalized frequency ρ	25
11. Variation of pulse time delay T with normalized operating frequency ρ at various values of take-off angle β_0	26
12. Shape of sweep-frequency, ground-backscattered echo bounded by its two extreme time delays as functions of ρ . β -Chapman Layer with no horizontal gradient	26
13. Shape of sweep-frequency, ground-backscattered echo bounded by its two extreme time delays as functions of ρ . β -Chapman Layer with horizontal gradient with $b/R = 0^\circ$	27
14. Shape of sweep-frequency, ground-backscattered echo bounded by its two extreme time delays as functions of ρ . β -Chapman Layer with horizontal gradient with $b/R = +30^\circ$	27

ILLUSTRATIONS (Cont'd)

Figure	Page
15. Shape of sweep-frequency, ground-backscattered echo bounded by its two extreme time delays as functions of ρ . β -Chapman Layer with horizontal gradient with $b/R = +60^\circ$. . .	28
16. Shape of sweep-frequency, ground-backscattered echo bounded by its two extreme time delays as functions of ρ . β -Chapman Layer with horizontal gradient with $b/R = -60^\circ$. . .	28
17. Determination of the back-scatter echo delay pattern (type A) from the T vs β_0 curve of Fig. 10	29
18. Type A backscatter echo pattern (range-amplitude) derived from the construction of Fig. 17	29
19. Shape of the ground-backscattered echo, bounded by its two extreme time delays (corresponding to minimum time delay and tangent rays) as functions of the normalized frequency ρ	31
20. Plots of electron density vertical distributions used in the calculations	32
21. Samples of continuous-sweep-frequency recordings showing various types of echoes	33
22. Signal flow and connection diagram of exciter-sounder	43
23. Occurrence of constant-range echoes	48
24. Plot of vertical angles β_0 at which downcoming rays meet geomagnetic field lines orthogonally in the E Layer at various distances due east and due west of Stanford	51
25. Statistical plot of the frequency of occurrence of constant range echoes against time of occurrence prevailing locally at the position of the irregularity	53
26. Geometry of the normal intersection of a downcoming ray with a geomagnetic field line looking west of Stanford	62

ACKNOWLEDGEMENT

The authors wish to thank: Prof. Allen M. Peterson for many valuable discussions on various aspects of the work; Mr. Alan A. Burns for the design and execution of the ray-tracing program on the analog computer; Mr. Douglas E. Westover for similar effort for the solution of the equivalent-path equation on the digital computer; and Messrs. Clair Powell and James V. Conklin for much help in carrying out the sounding experiments.

The research work was jointly sponsored by the Office of Naval Research under contract Nonr 225(64) and the National Academy of Sciences, Washington, D. C., through a National Research Council Fellowship to Dr. S. N. Denno, who is on leave of absence from the University of Baghdad, Iraq.

SYMBOLS

b	ground distance between transmitter and subsolar point
c	velocity of light in free space
f_o	maximum frequency at which ray will be reflected at peak electron density N_o in layer (critical frequency)
f_{ob}	wave frequency at oblique propagation
f_v	wave frequency at vertical propagation
h	true height of ray reflection in the F layer (in ray tracing h and x were used as the rectangular coordinates of the ray path)
h_o	height of bottom of ionosphere (F layer of parabolic distribution)
h'	virtual height of ray reflection
$k_{\phi o}$	correction factor for curvature of ionosphere
v_g	group velocity of propagated wave
y	ground distance of ray from subsolar point
y_m	half thickness of ionosphere (F layer of parabolic distribution)
z	normalized height used in Chapman formula for ion-density distribution, equal to $(h - h_{max})/H$
A	angle between ray-path plane and magnetic-north direction at a point in the path at E-layer height
D	geomagnetic-declination angle at E-layer height. Also ground distance covered by ray between transmitter and scattering point on ground
$F(h)$	vertical-distribution function of electron density in F layer
I	geomagnetic-dip angle at E-layer height
N	electron-number density in ionosphere (F layer)
N_o	peak electron-number density in F layer
P'	total length of equivalent group path of ray between transmitter and scattering point on ground, i.e., oblique distance of scattering point

SYMBOLS (Cont'd)

P'_{\min}	length of oblique distance corresponding to minimum delay time (close to skip distance)
R	earth's radius (6367 km)
S	total length of true group path of ray between transmitter and scattering point on ground
$S(x)$	horizontal-distribution function of electron density in F layer along ray path
$S(y)$	horizontal-distribution function of electron density in F layer in a meridian plane containing subsolar point and a point in ray path
T	total one-way group delay of ray between transmitter and scattering point on ground
α	angle between the two meridian planes containing propagated ray and a geomagnetic field line at E-layer height, respectively
β_0	initial vertical angle of propagated ray
β_p	vertical angle of downcoming ray at E-layer height after reflection by F layer
μ	phase-refractive index at any point in ionospheric layer supporting propagation
ρ	normalized frequency, equal to f/f_o , where f is frequency of propagated wave. For ground backscattering $f = f_{ob}$
ϕ_0	angle of incidence of ray at the point of virtual reflection in the ionosphere
χ	zenith angle of sun's rays incident on ionosphere
θ	angle at earth's center subtended by arc distance D

I. INTRODUCTION

The work reported here is an analysis of the ground-backscatter echo, with particular reference to the effect of continuous variation of frequency and the appearance of certain echoes that seem to be unaffected by this variation, thus appearing as constant-range echoes.

It is now well established that, when a pulse of radio frequency is propagated obliquely via the ionosphere, an echo is received after a certain time delay as a result of scattering from irregularities on the distant earth's surface, be it land or sea, providing that one or more of the ionospheric layers can support such propagation. If the pulse length is of the order of 1 msec, the nature of the scattering irregularities seems to have a secondary effect on the strength of the pattern formed by the received echoes [Ref. 1]. Thus, whether the beam is directed towards water or dry land, the pattern is governed primarily by the prevailing structure of the ionosphere. Furthermore, because of the random distribution of the scattering irregularities, the received echo is phase incoherent; but nevertheless, it is possible to employ the principles of simple ray theory in the analysis of the transmission mechanism.

II. CHARACTERISTICS OF THE BACKSCATTER ECHO

A. THE REFLECTED ECHO AND ITS PRESENTATION

When a radar pulse is transmitted from an isotropic radiator, the shape of the returning echo, after being reflected twice by the ionosphere and scattered once by the ground, is governed by the time delay of each ray component and the density of these components at any particular moment. The original shape of the pulse is thus completely lost [Ref. 2]. The analysis follows each ray separately along its group path, treating it as an individual pulse of infinitesimal duration with application of the laws of oblique transmission. Hence the characteristics of the ionosphere present along the ray path have a primary effect on this shape.

The backscatter echo may be presented in an A-scope display relating received field strength and time delays, or by using the electron-beam modulation of a cathode-ray tube as a third dimension. The above relationship can be extended to show the variation of the echo as a function of time or frequency.

B. GROUP PATH AND TIME DELAY

The aforementioned display gives the delay of the echo, $2T$, which is the time taken for the pulse to make the round trip before it is received as an echo. It is assumed here that the actual group path S followed by the ray in the outgoing direction is the same as that followed in the return direction; hence, for simplicity, we shall consider in our analysis one-way conditions only. Since the ionosphere is geographically non-homogeneous, the phase-refractive index μ and therefore the velocity of propagation will be functions of space. For a group velocity v_g the time delay is given by

$$T = \int \frac{ds}{v_g}, \quad (1)$$

and, when the effects of the earth's magnetic field and collisional damping are neglected, the time delay can be expressed in terms of the phase refractive index as

$$T = \frac{1}{c} \int \frac{ds}{\mu}, \quad (2)$$

where c is the velocity of electromagnetic waves in vacuum.

The concept of the equivalent path is very useful in sounding work and, in this case, the equivalent-group path P' simply replaces the integral term in Eq. (2). Thus,

$$T = \frac{P'}{c}. \quad (3)$$

Figure 1 shows the geometry of the equivalent path for curved earth condition. B is a point of assumed specular reflection at an equivalent height h' in the ionosphere. Under flat-earth conditions, the equivalence theorem relates P' and h' by the equation

$$h' = \frac{P'}{2} \cos \phi_0, \quad (4)$$

where ϕ_0 is the angle of incidence of the ray at the bottom of the

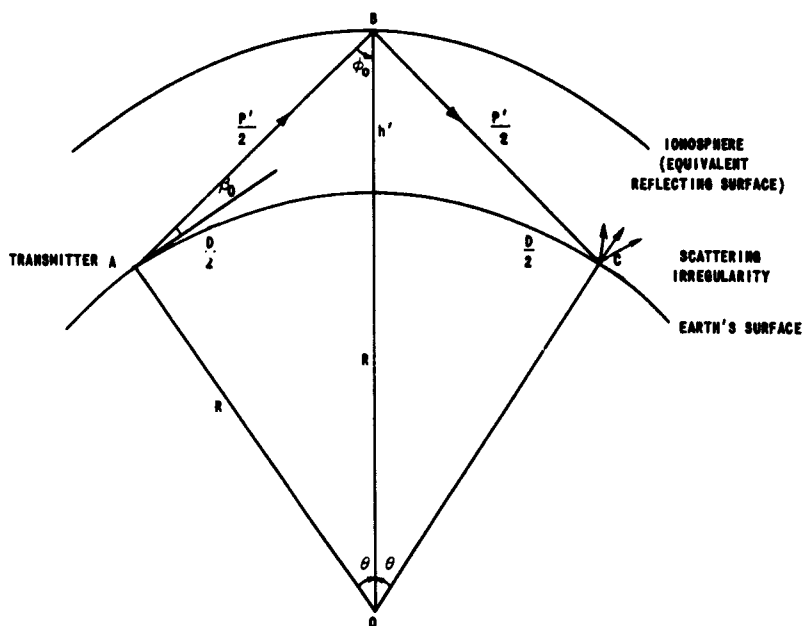


FIG. 1. GEOMETRY OF EQUIVALENT RAY PATH.

ionosphere and is also the half-vertex angle of the equivalent triangular path.

The curvature of the earth and ionosphere requires modification of the plane geometry as well as the so-called secant law on which the equivalence theorem is based. Smith [Ref. 3] has shown that, in the case of the ionosphere following the curvature of the earth's surface (radius R) with a lower boundary at a constant height h_0 above it, the true relationship between the oblique-incidence frequency f_{ob} and the equivalent vertical-incidence frequency f_v for which h' is the vertical height is given by

$$f_v = f_{ob} \cos \phi_0 \left[1 - \frac{2(h' - h_0)}{(R + h_0)} \tan^2 \phi_0 \right]^{\frac{1}{2}} \quad (5a)$$

$$= f_{ob} (\cos \phi_0) k_{\phi_0}, \quad (5b)$$

where h is the real height at which the actual ray trajectory reaches at its apex.

Note that the angle ϕ_0 remains to be half the vertex angle of the triangle ABC, but in this case it is smaller than the angle of incidence at the bottom of the ionosphere.

It will also be noticed that the effect of the factor k_{ϕ_0} in Eq. (5b) is to lower the equivalent vertical-incidence frequency or what amounts to the lowering of the virtual height of vertical incidence, which can readily be seen from the curved geometry.

It is sometimes more convenient to express the above relationships in terms of the take-off angle β_0 ; for the curved-earth condition, as shown in Appendix A, the equivalent path is given by

$$P' = 2 \{ [(R + h')^2 - R^2 \cos^2 \beta_0]^{\frac{1}{2}} - R \sin \beta_0 \}. \quad (6)$$

For a layer of parabolic electron distribution of half thickness y_m , the value of h' can be derived from Eq. (A.12) of Appendix A, which is in a form amenable to simple solution by a digital computer.

C. THE EQUIVALENT PATH APPROACH

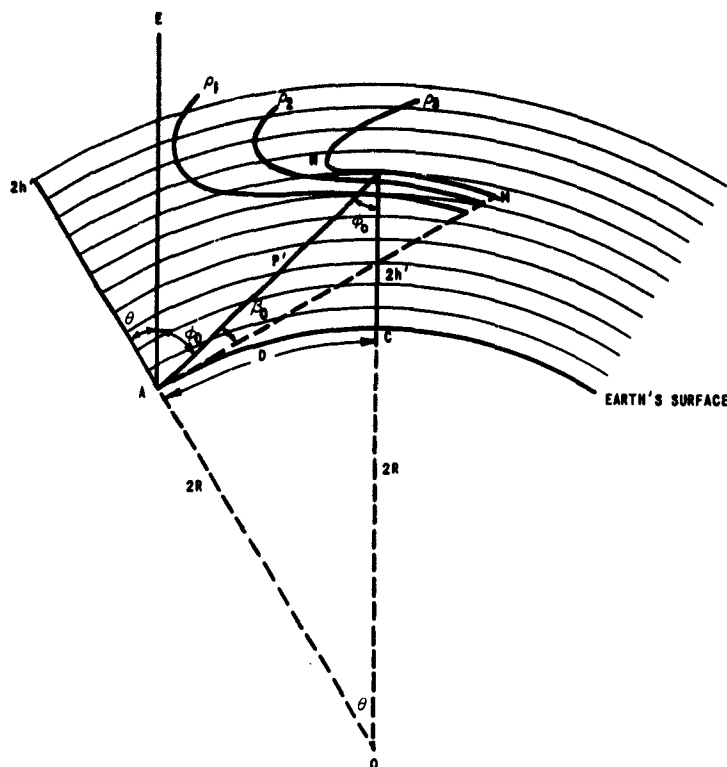
The study of the characteristics of the ground backscatter echo is first made by utilizing the concept of the equivalent-group path, for which it is necessary to assume a certain ion-distribution model of the reflecting layer.

A useful graphical method for this study is that developed by Peterson [Ref. 4], which shows, in combined rectangular-polar coordinate systems, the relationship between take-off angle β_o , equivalent-group distance or oblique path P' , virtual height of reflection h' , and horizontal ground distance to the point of ground reflection D . The curve relating these quantities, which may be called the reflectrix,^{*} is drawn parametric with the operating frequency f_{ob} which is usually normalized with respect to the vertical-incidence critical frequency of the ionospheric layer f_c . This treatment, however, was confined to the case of flat earth and flat ionosphere, and its accuracy is therefore limited to short ranges. For longer ranges, the curved geometry shown in Fig. 1 should be taken into consideration, and Peterson's construction can still be applied with the same coordinate system, for a given ionospheric electron distribution. The shape of the reflectrix, i.e., the locus of the extremity of the line, (in this case curved) representing the length of the equivalent path, however, will be quite different.

Alternatively, the construction can be made more realistic by using a circular coordinate system as shown in Fig. 2. The ground range D corresponding to any point on the reflectrix will be measured by the radial projection along a circle of radius $2R$, where R is the earth's radius, thus keeping the angular relationship of the transmission geometry the same, with a linear representation of distances h' and P' . Good approximation may be obtained by simply drawing the plane-earth data on the circular coordinates.

Since the length of the equivalent path P' is proportional to the time delay T (Eq. 3) the construction in Fig. 2 facilitates the

^{*}The term, originally devised by Lejay and Lepechinsky [Ref. 5], applied to the locus of the virtual point of the first reflection in the ionosphere. As it will be used here, the reflectrix involves double the distances and the same angles.



study of the shape of the backscatter echo by following the variation of P' along any of the reflectrices shown. For any normalized frequency ρ , the width of the echo, i.e., its duration, will fall between points such as N and M. The former, at the tip of the reflectrix, is the point of minimum time delay, and the latter corresponds to the maximum length of path at zero-angle propagation. Furthermore, the rate of change of the length of P' with respect to the angle β_0 gives a measure of the amplitude of the echo, so that, at any value P' or its equivalent delay T , the echo intensity depends to a first order on $1/(dP'/d\beta_0)$. It is obvious that the point of minimum time delay produces the highest amplitude in the echo, resulting from what is known as minimum-time-delay focussing.

It will also be noticed that, unlike the flat earth case, the intensity of the echo corresponding to zero take-off angle has a finite value, as can be seen from the value of $dP'/d\beta_0$ (derived in Appendix A), which reaches a limiting value of $(-2R)$ because of the low penetration at such low angles (Eq. A.15). This will later be referred to as the limit, or tangent-ray echo.

Using this construction, Eq. (6) is plotted for a typical parabolic layer of maximum ionization height of 300 km and semi-thickness of 100 km. The result is shown in Fig. 3. No correction was made in this case for the curvature of the ionosphere at the point of assumed reflection. Thus the factor k_{ϕ_0} was, for simplicity, made equal to unity.

In the type of display used in the present experiments--namely, range vs frequency, with intensity modulation representing the strength of the received echo--the pattern produced (called the Sweep Frequency Echo, SFE) for a given frequency range is bounded by two extreme echoes identifying the two rays referred to earlier--namely, the minimum-time-delay and the tangent ray. It is therefore useful to single out these rays and show their variation with frequency, which is presented in the plot of Fig. 4, taken from the construction of Fig. 3 after suitable conversion of the equivalent-group paths into one-way time delays.

D. THE RAY-TRACING APPROACH

1. General

A more realistic, though involved, approach to the determination of time delay and the prediction of the shape of the received echo is by means of ray-tracing techniques. The actual path of the electromagnetic-wave energy, which is the true group path, is followed along the non-uniform electron concentration of the ionosphere from the point of departure at the transmitter. Thus it is possible for a study to be made when horizontal gradients or, in fact, any form of electron-density distribution exist.

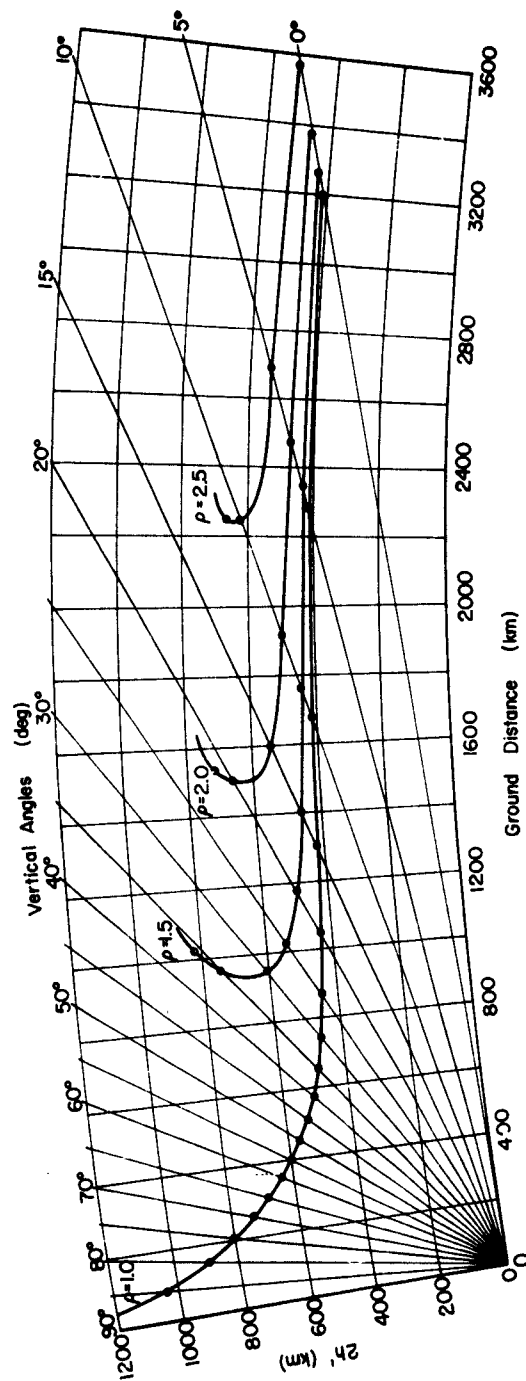


FIG. 3. EQUIVALENT PATH P' AND HEIGHT h' AT ELEVATION ANGLES β_0 AND NORMALIZED FREQUENCIES ($\rho = f_{0b}/f_c$) OF 1.0, 1.5, 2.0, AND 2.5, FOR A PARABOLIC F LAYER OF $h_0 = 200$ km AND $y_m = 100$ km, USING EQS. (7) AND (12) OF APPENDIX A.

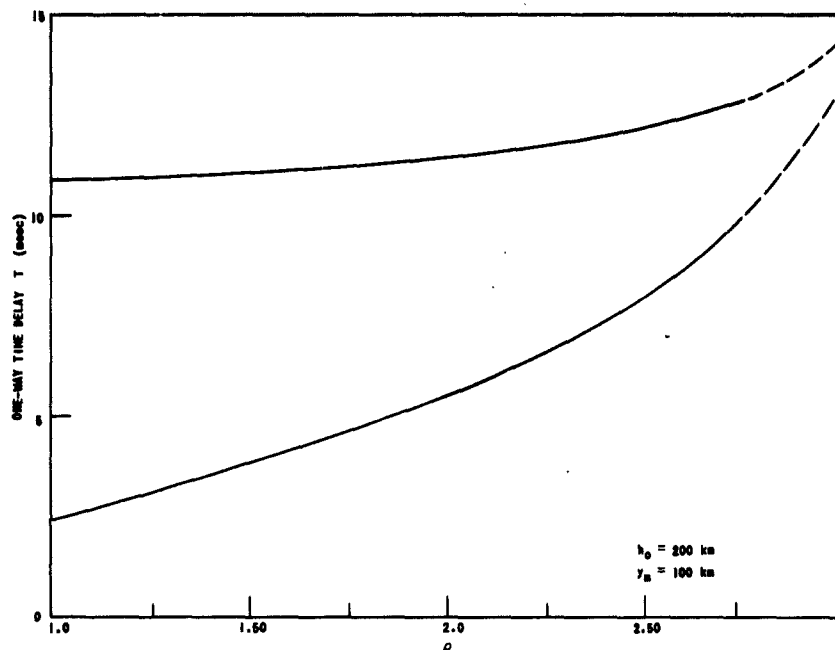


FIG. 4. SHAPE OF SWEEP-FREQUENCY, GROUND-BACKSCATTERED ECHO, BOUNDED BY ITS TWO EXTREME TIME DELAYS AS FUNCTIONS OF THE NORMALIZED FREQUENCY. Parabolic layer $h_0 = 200$ km, $\gamma_m = 100$ km.

2. Ray Tracings with a β -Chapman Layer

An analog computer was programmed to solve the following equation from ray theory [Ref. 6], based on Snell's law and Fermat's principle of stationarity, for curved earth and curved isotropic ionosphere in a two-dimensional coordinate system

$$\frac{d^2 h}{dx^2} = \left[\left(1 + \frac{h}{R} \right)^2 + \left(\frac{dh}{dx} \right)^2 \right] \frac{1}{\mu} \left(\frac{\partial \mu}{\partial h} \right) + \left[\left(1 + \frac{h}{R} \right)^2 + 2 \left(\frac{dh}{dx} \right)^2 \right] \frac{1}{R + h} - \left[1 + \left(1 + \frac{h}{R} \right)^{-2} \left(\frac{dh}{dx} \right)^2 \right] \frac{1}{\mu} \left(\frac{dh}{dx} \right) \left(\frac{\partial \mu}{\partial x} \right) \quad (7)$$

where: h = real height above the earth's surface at any arc distance x from the transmitter

μ = phase-refractive index.

In the programming of the analog computer, two approximations were made to simplify the above equation for more efficient use of the computer.

1. Since $h \ll R$,

$$\left(1 + \frac{h}{R}\right)^2 \approx 1 + \frac{2h}{R}, \quad (8)$$

and, in the second term of Eq. (7),

$$(R + h) \approx R. \quad (9)$$

2. Because of the small variation of the refractive index in the horizontal direction, the last term of Eq. (7) is neglected, leaving the terms for the vertical gradient and the earth's curvature. However, the effect of the horizontal gradient of the electron density is not completely dropped, since it appears in the following evaluation of the refractive index in terms of frequency,

$$\mu^2 = 1 - \frac{N(h, x)}{1.24 \times 10^4 f_{ob}^2}, \quad (10)$$

where $N(h, x)$ is the electron-number density per cubic centimeter along any particular ray path.

If N_0 is the maximum electron density present in the layer, the electron density at any other point (h, x) can be expressed in terms of a vertical and horizontal components, $F(h)$ and $S(x)$ respectively, of the spatial distribution function. Thus,

$$N(h, x) = N_0 \cdot F(h) \cdot S(x). \quad (11)$$

Hence,

$$\mu^2 = 1 - \frac{N_0}{1.24 \times 10^4 \times f_{ob}^2} F(h) S(x). \quad (12)$$

The concentration N_0 will correspond to a critical frequency f_0 Mc/s at vertical incidence such that $N_0 = 1.24 \times 10^4 f_0^2$, giving,

for the refractive index,

$$\mu^2 = 1 - \frac{r_o^2}{r_{ob}^2} F(h) \cdot S(x) \quad (13)$$

or

$$\mu^2 = 1 - \frac{F(h) \cdot S(x)}{\rho^2} \quad (14)$$

The functions $F(h)$ and $S(x)$ were produced in the analog computer by means of function generators of the diode type. For the vertical direction, a β -Chapman distribution was assumed for the F layer [Ref. 7] with a height of maximum ionization of 300 km and a scale-height of 100 km. Thus,

$$F(h) = \exp [1 - z - \exp(-z)], \quad (15)$$

where

$$z = (h - 300)/100. \quad (16)$$

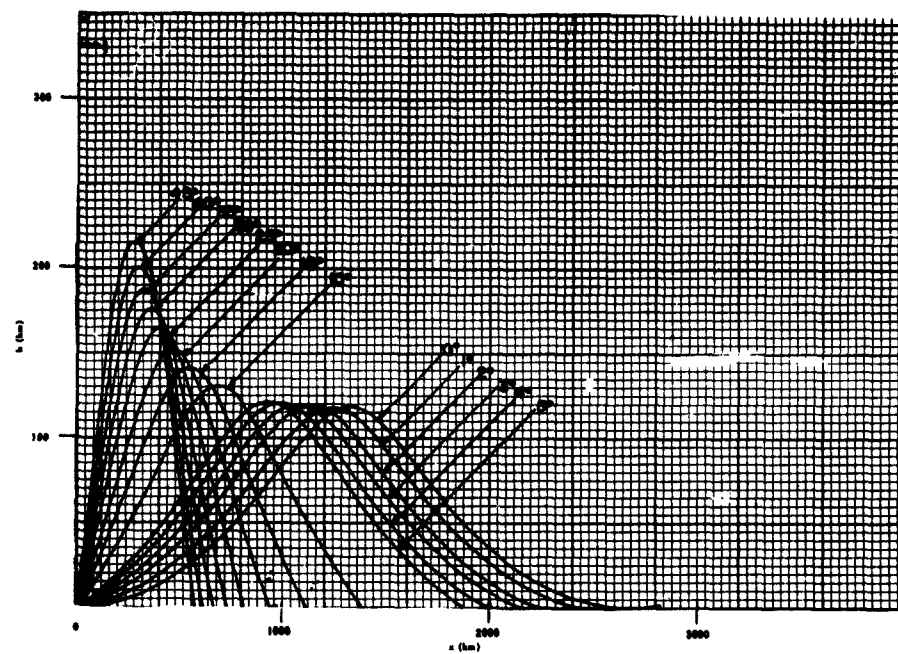
The horizontal gradient $S(x)$ of the spatial-distribution function is taken as unity for the sample ray-path tracings shown in Fig. 5. A cosine function was also introduced to simulate the effect of the sun's zenith angle χ over the various portions of the ionosphere along the path. This function provides a rough approximation to what, even theoretically, is considered to happen since, although the peak electron density of the β -Chapman layer is proportional to the cosine of the zenith angle, i.e.,

$$N_o = [N_o]_{\chi=0} \cdot \cos \chi, \quad (17)$$

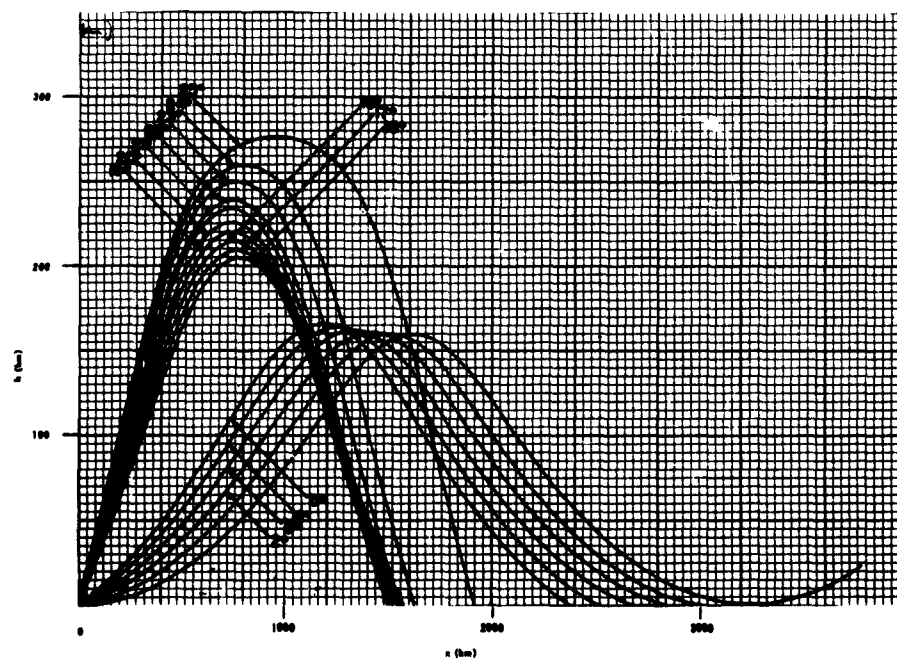
the height of this peak does not remain constant but rather increases with this angle and occurs at

$$z_{\chi} = \ln \sec \chi, \quad (17a)$$

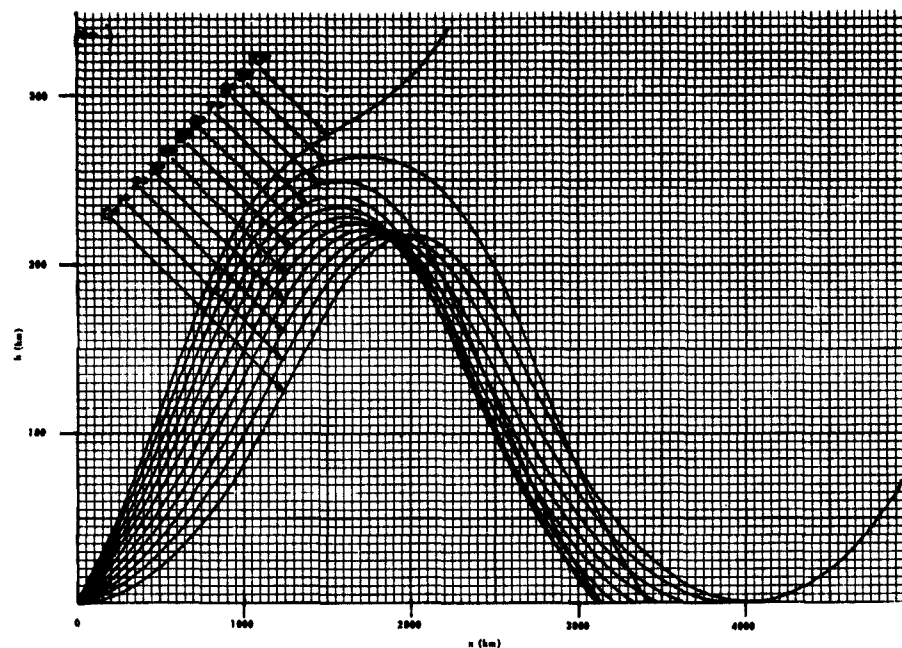
which is ignored in the present computation.



a. From 0° to Critical at 46° ; $\rho = 1.0$.



b. From 0° to Critical at 26° ; $\rho = 2.0$.



c. From 0° to Critical at 10° ; $\rho = 3.0$.

FIG. 5. TRACINGS OF RAYS OF VARIOUS TAKE-OFF ANGLES IN A β -CHAPMAN LAYER. $S(x) = 1$.

Hence, at any point along the ray path whose projection on the ground is distant y km from the subsolar point, the value of the electron density gradient formed is

$$S(y) = \cos (y/R). \quad (18)$$

In Appendix B the trigonometry of this general case is given. It is also shown that, for the case in which the transmitter, the subsolar point, and the ray path fall in the same meridian plane,

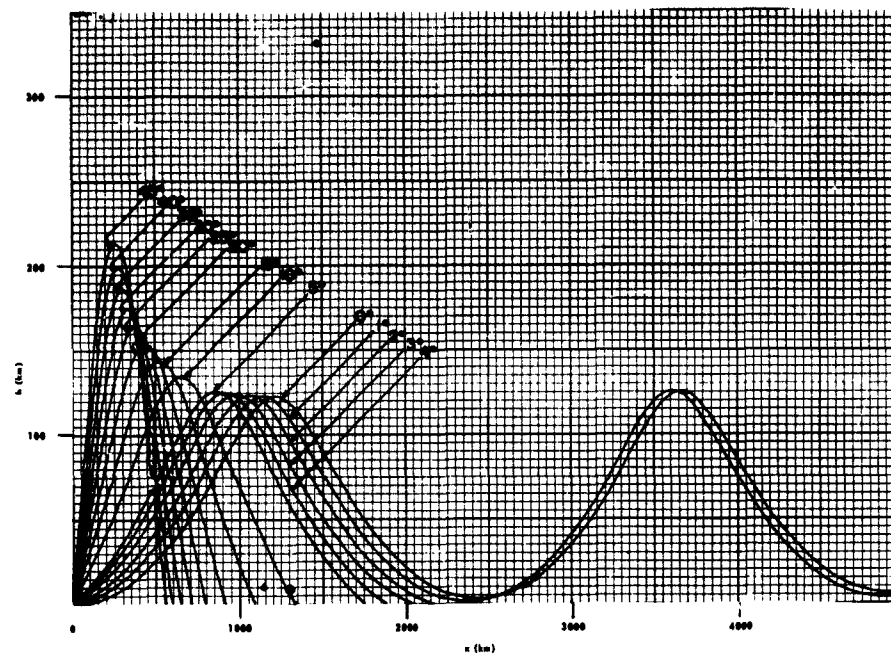
$$S(x) = \cos (y/R) = \cos \left(\frac{x}{R} - \frac{b}{R} \right), \quad (19)$$

where b is the ground distance between the transmitter and the subsolar point. Note that the frequency represented by ρ remains normalized with respect to the critical frequency of the maximum ion density, which in this case will be over the subsolar point. Ray tracings for this case were made with the sun at different zenith angles from the transmitter, viz., 0° , $+30^\circ$, $+60^\circ$ for b equal to 0, 3333, 6667, and -6667 km, respectively, and are shown in Figs. 6 through 9. These would correspond to conditions during different hours of the day, depending upon latitude and direction of propagation.

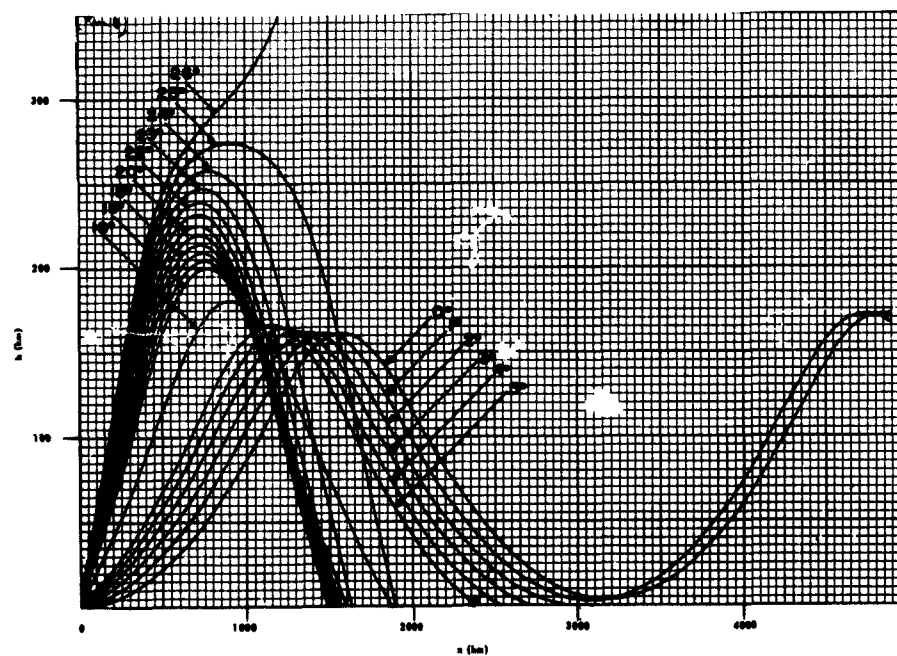
The ray tracings obtained are for different normalized frequencies ρ and initial angles of propagation β_0 given by

$$\beta_0 = \tan^{-1} \left[\frac{dh}{dx} \right]_{x=0}. \quad (20)$$

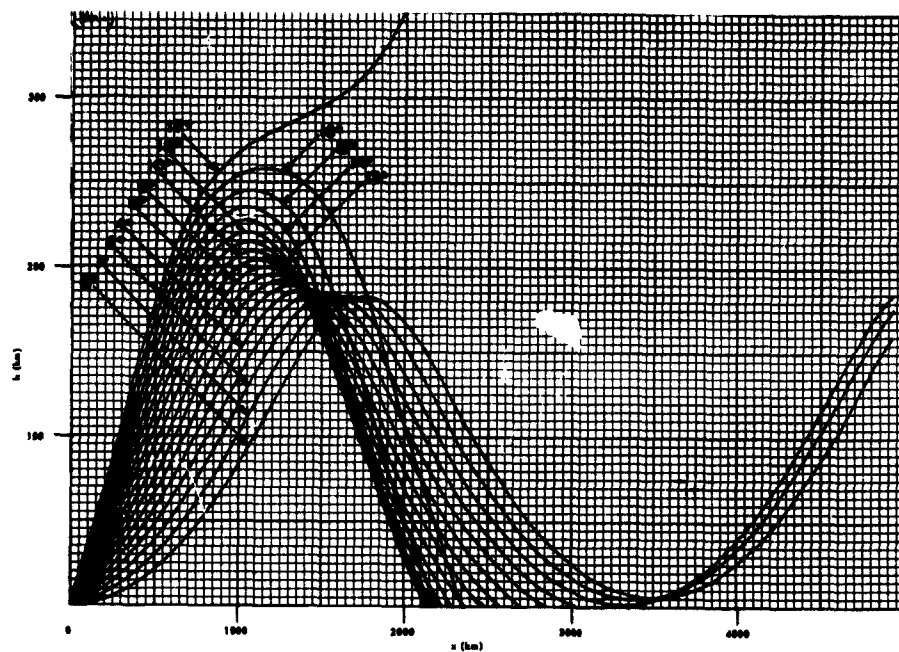
This page is blank.



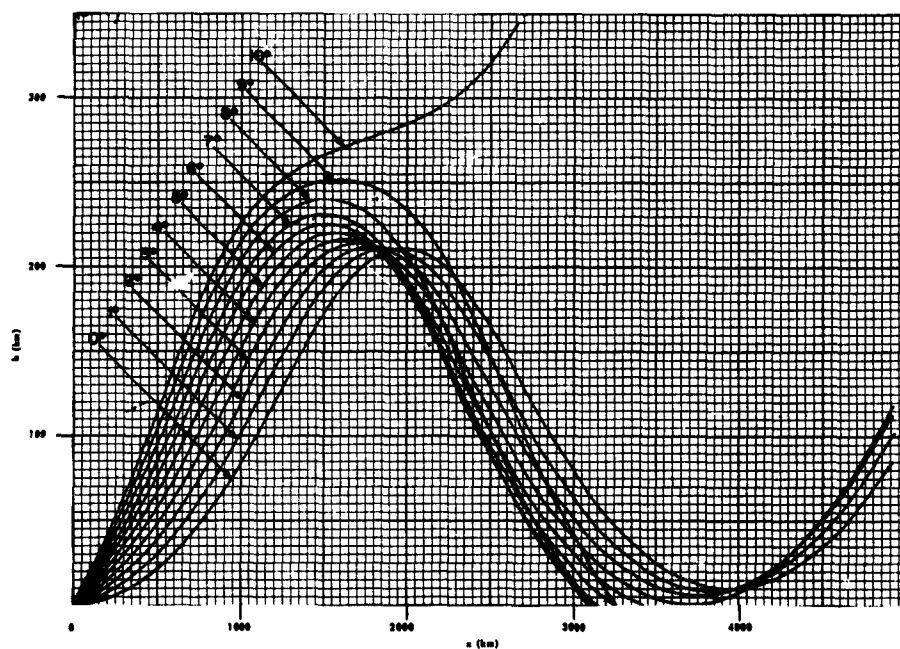
a. From 0° through Critical at 46° ; $\rho = 1.0$.



b. From 0° through Critical at 26° ; $\rho = 2.0$.

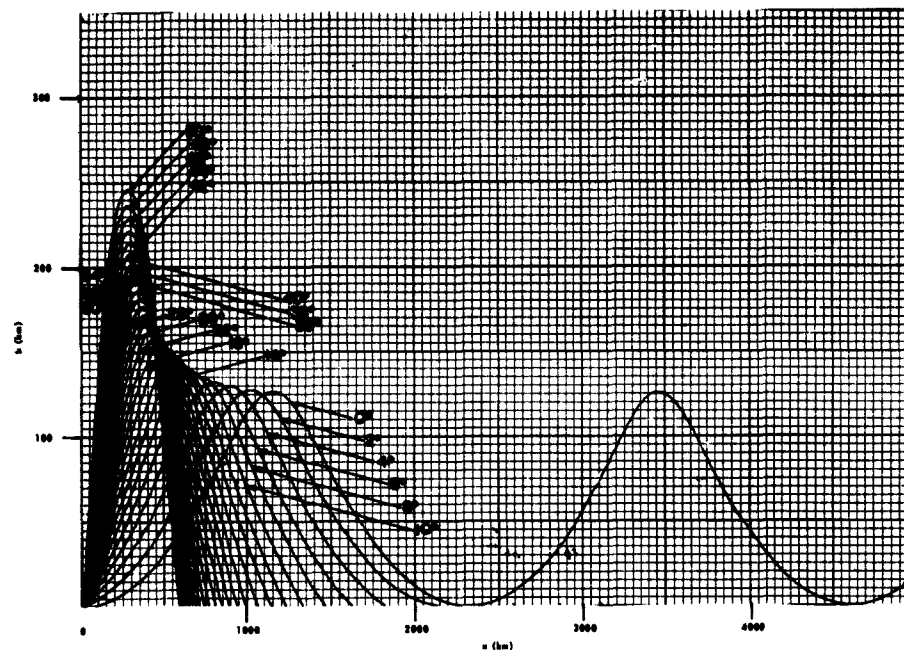


c. From 0° through Critical at 17° ; $\rho = 2.5$.

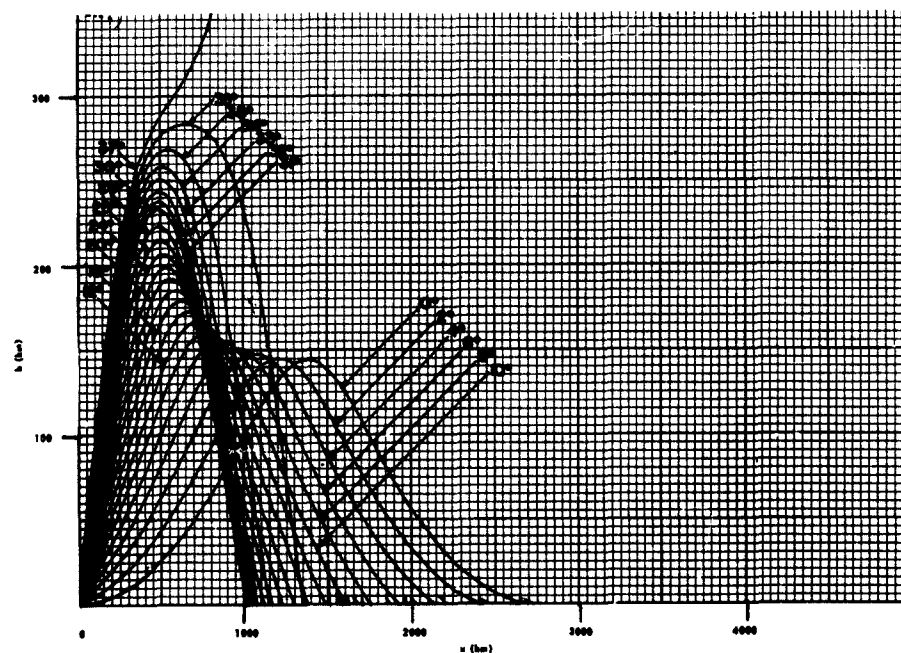


d. From 0° through Critical at 10° ; $\rho = 3.0$.

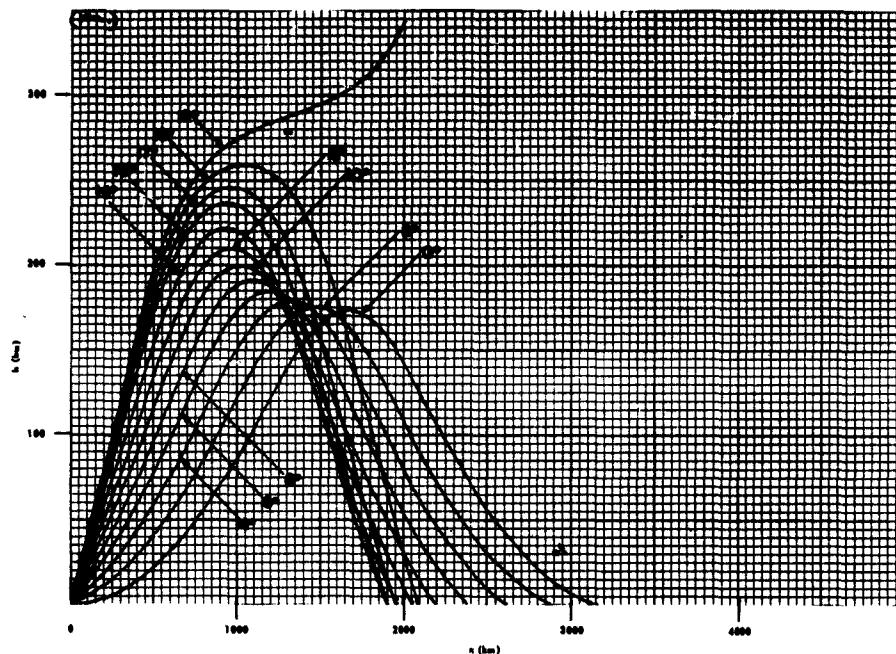
FIG. 6. TRACINGS OF RAYS OF VARIOUS TAKE-OFF ANGLES
IN A β -CHAPMAN LAYER. $S(x) = \cos [(x-b)/R]$; $b = 0$ km.



a. From 0° through Critical at 51° ; $\rho = 1.0$.

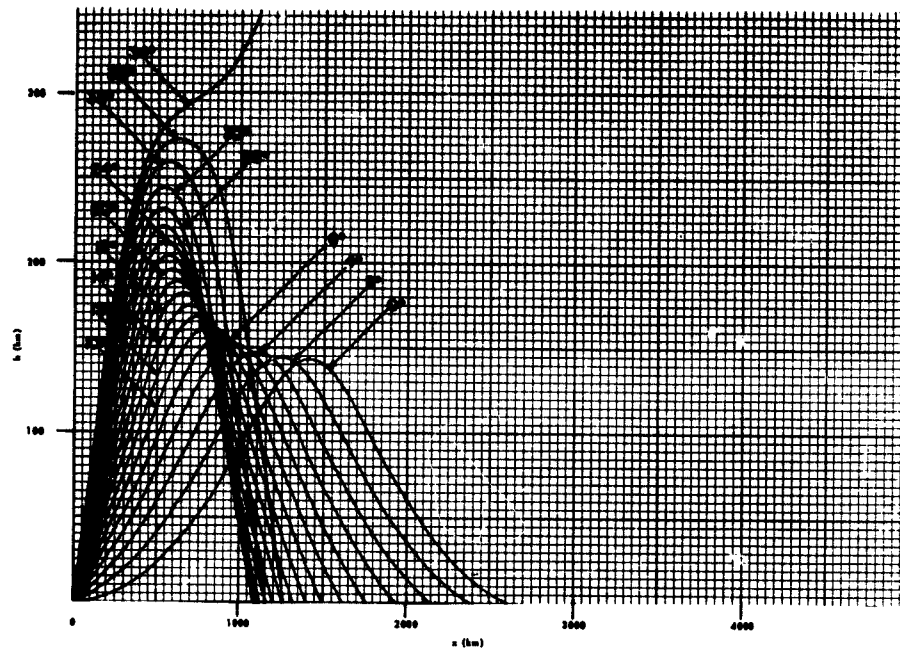


b. From 0° through Critical at 37° ; $\rho = 1.5$.

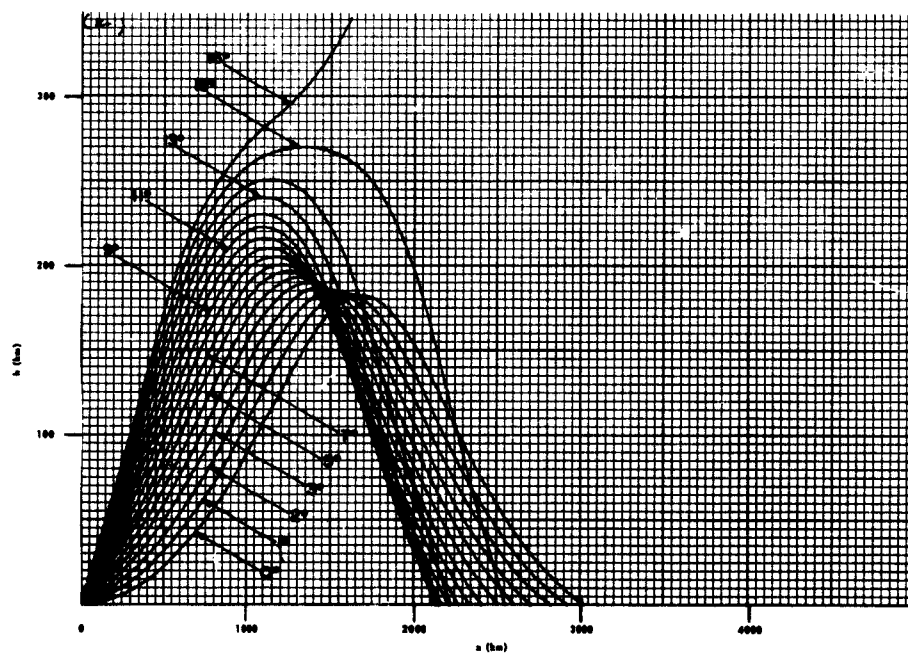


c. From 0° through Critical at 19° ; $\rho = 2.25$.

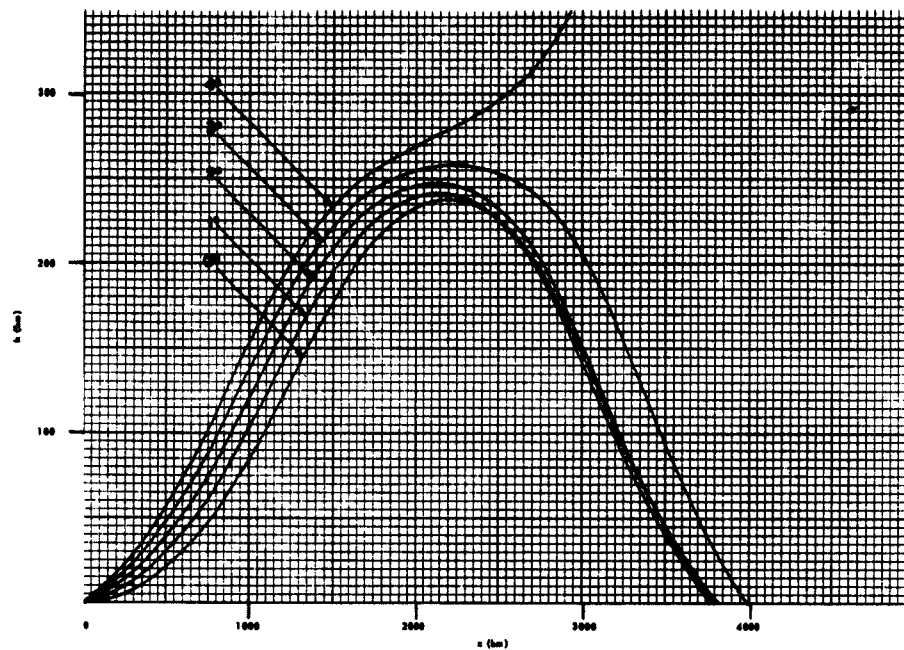
FIG. 7. TRACINGS OF RAYS OF VARIOUS TAKE-OFF ANGLES
IN A β -CHAPMAN LAYER. $S(x) = \cos [(x-b)/R]$; $b = 3333$ km.



a. From 0° through Critical at 34° ; $\rho = 1.25$.

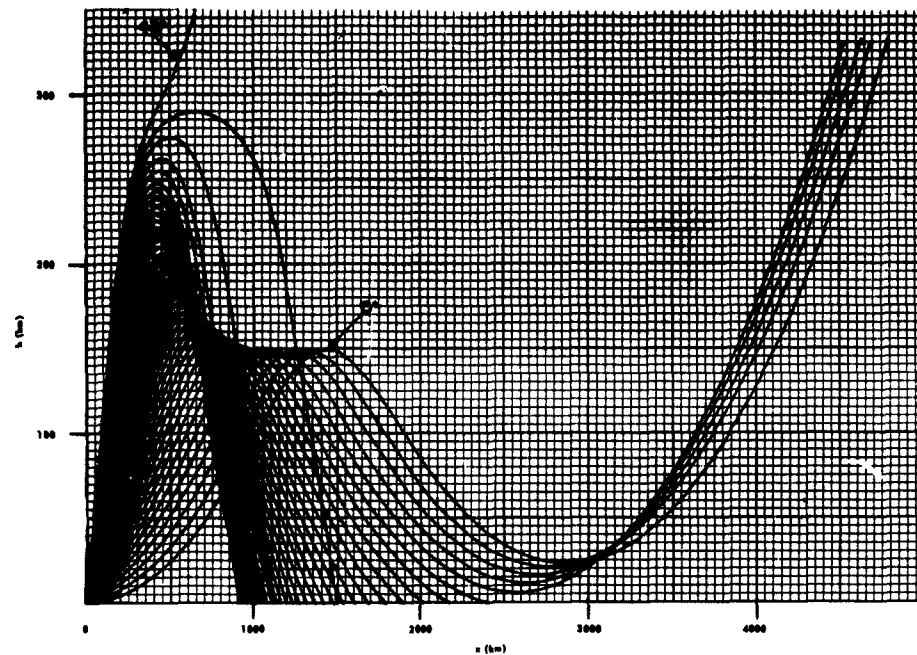


b. From 0° through Critical at 16° ; $\rho = 2.0$.

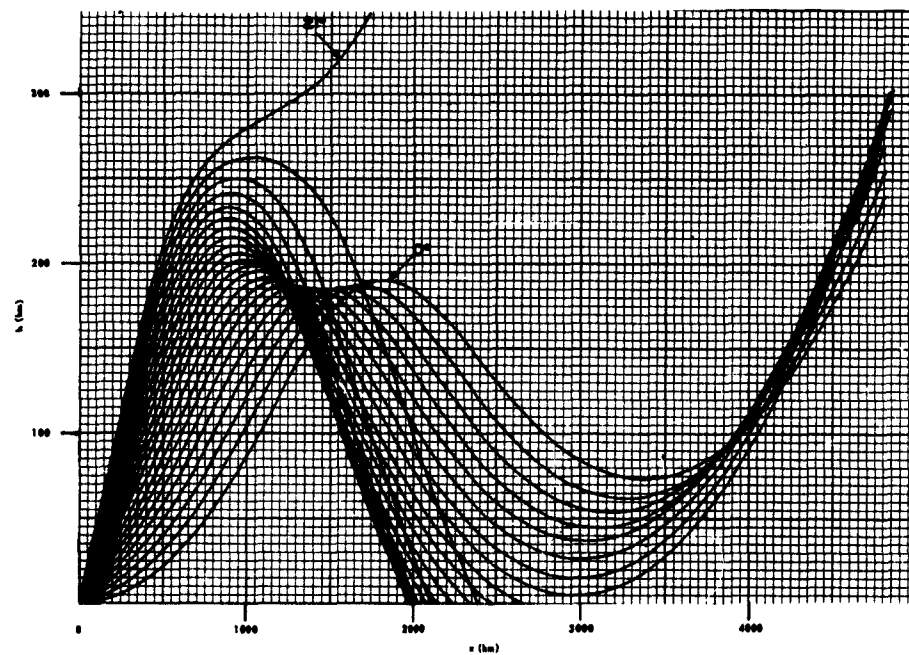


c. From 0° through Critical at 4° ; $\rho = 2.75$.

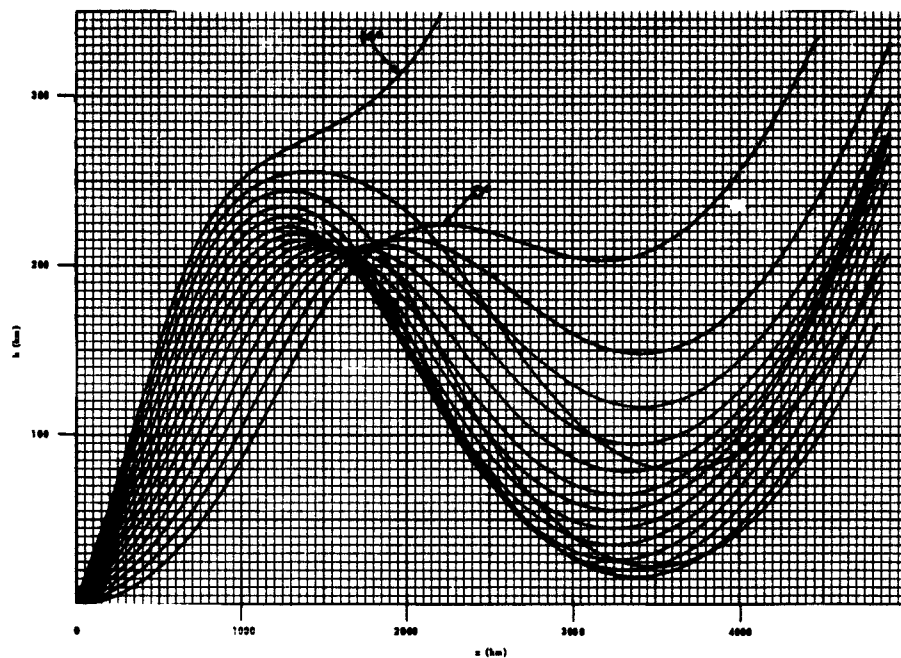
FIG. 8. TRACINGS OF RAYS OF VARIOUS TAKE-OFF ANGLES
IN A β -CHAPMAN LAYER. $S(x) = \cos [(x-b)/R]$; $b = 6667$ km.



a. Between 0° and 43° (Critical); $\rho = 1.0$.



b. Between 0° and 21° (Critical); $\rho = 1.5$.



c. Between 0° and 14° (Critical); $\rho = 1.75$.

FIG. 9. TRACINGS OF RAYS OF VARIOUS TAKE-OFF ANGLES
IN A β -CHAPMAN LAYER AT 1-deg INTERVALS. $S(x) =$
 $\cos [(x-b)/R]$; $b = -6667$ km.

3. Derivation of Time Delay and Its Relation to the Backscatter Echo

The determination of the group time delay is obtained from the computer loop by tapping off the variables (dh/dx) and μ and sub-programming Eq. (21) (see Appendix C)

$$T = \frac{1}{c} \int_{x=0}^{h=0} \frac{\left[1 + \left(\frac{dh}{dx} \right)^2 \right]^{1/2}}{\mu} dx, \quad (21)$$

to obtain the one-way delay time for the pulse between the transmitter and the point of contact with the ground.

For the case of $S(x) = 1$, these time delays are plotted in Fig. 10 as a function of the take-off angle and parametric with the normalized frequency ρ , and in Fig. 11 as function of ρ and parametric with β_0 . The latter figure illustrates the caustic focusing that takes place at minimum time-delay and forms the boundary or envelope of the sweep-frequency backscatter echo. This envelope, together with that produced by $\beta_0 = 0$, are redrawn in Fig. 12 for comparison with that of Fig. 4, which was obtained for a parabolic ion distribution by the equivalent-path method.

This latter type of presentation of the time-delay results is repeated for the other conditions of the horizontal gradient and is shown in Figs. 13 through 16.

Finally, as a means of predicting the approximate shape of the intensity distribution of the backscatter echo, a histographic plot is made, from the T vs β_0 curve (Fig. 10) of the relative number of rays that contribute towards each time-delay step or interval. Assuming an isotropic radiation pattern for the antenna and, for first order approximation, disregarding the effect of distance traveled by each ray, the number of rays (and hence the echo-signal intensity) with any specified delay interval such as ΔT between T_1 and T_2 in Fig. 17 will be proportional to the angle enclosed within that interval, viz., $(\Delta\beta_l + \Delta\beta_h)$ covering both the low and the high rays. Figure 18 shows a sample histographic plot taken from one of the curves in Fig. 10 for $\rho = 2.25$. The time interval ΔT was taken as 0.25 msec. The term "angular spread" refers to the sum $(\Delta\beta_l + \Delta\beta_h)$ in degrees.

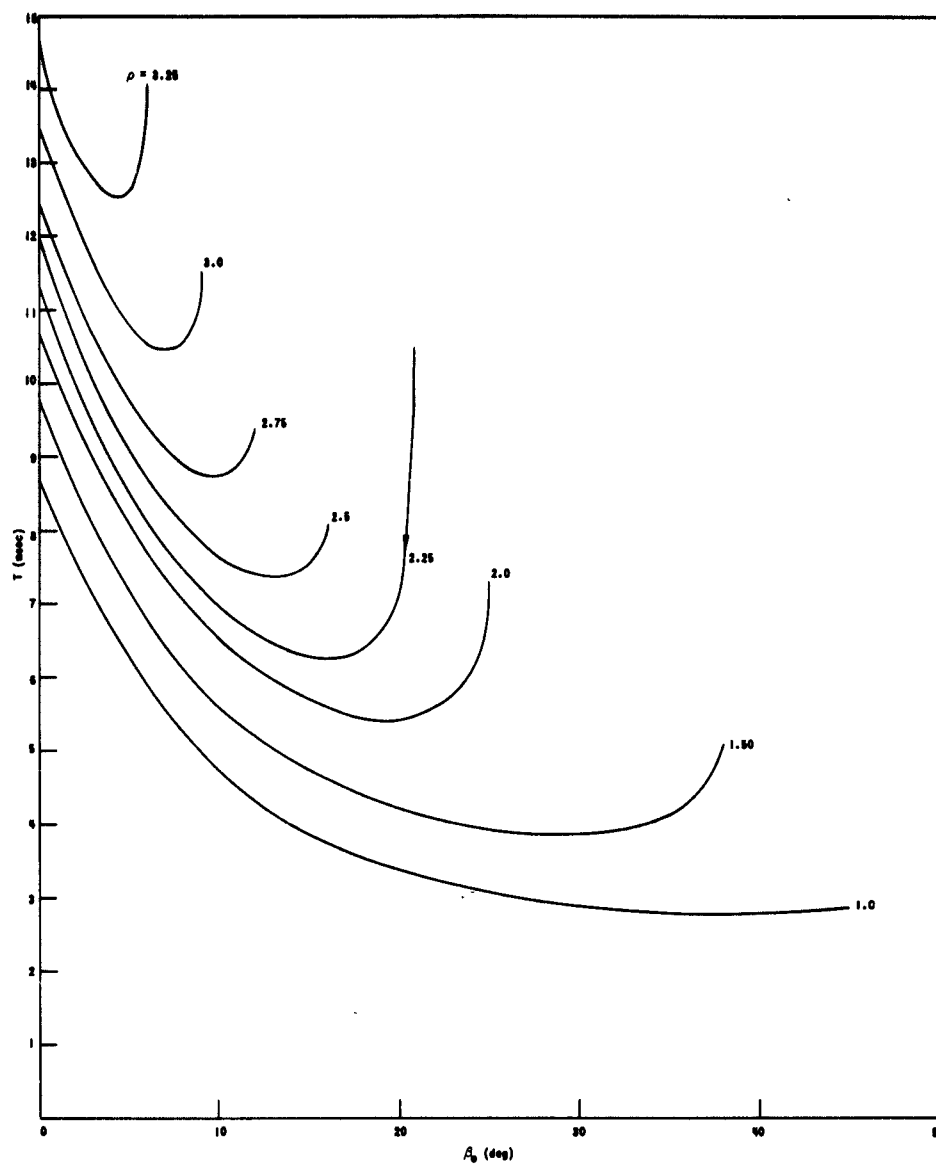


FIG. 10. VARIATION OF PULSE TIME DELAY T WITH TAKE-OFF ANGLE β_0 AT VARIOUS VALUES OF NORMALIZED FREQUENCY ρ . THE VALUES OF T ARE OBTAINED FROM THE ANALOG COMPUTER THROUGH EQ. (21). β -CHAPMAN LAYER OF $h_{\max} = 300$ km, $H = 100$ km, WITH NO HORIZONTAL GRADIENT OF ELECTRON DENSITY.

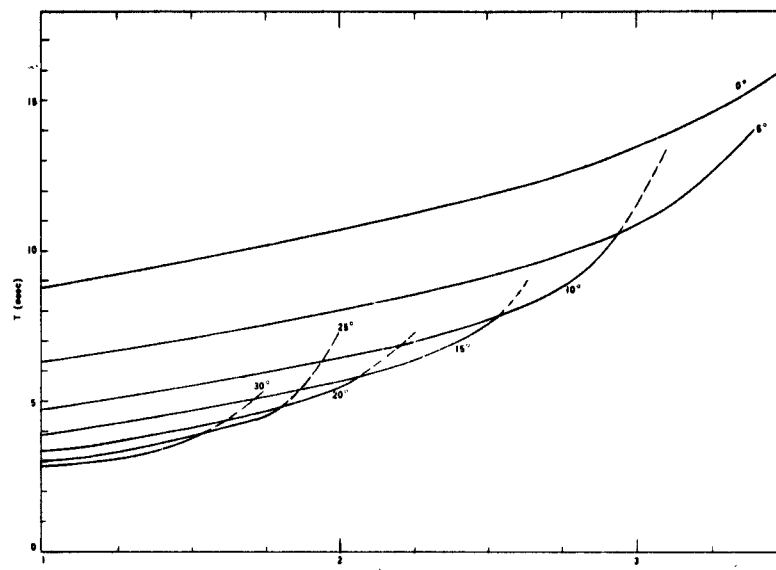


FIG. 11. VARIATION OF PULSE TIME DELAY T WITH NORMALIZED OPERATING FREQUENCY ρ AT VARIOUS VALUES OF TAKE-OFF ANGLE β_0 . Same layer conditions as those of Fig. 10.

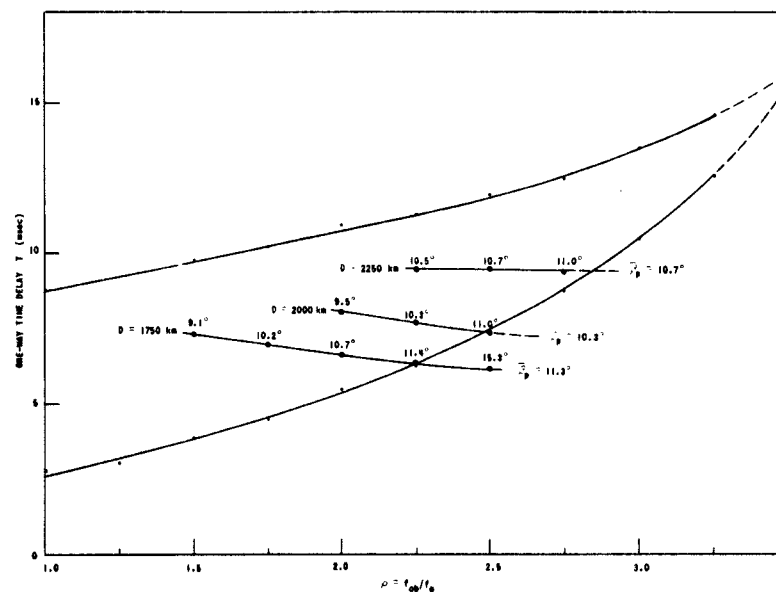


FIG. 12. SHAPE OF SWEEP-FREQUENCY, GROUND-BACKSCATTERED ECHO BOUNDED BY ITS TWO EXTREME TIME DELAYS AS FUNCTIONS OF ρ . β -Chapman layer of $h_{\max} = 300$ km, $H = 100$ km with no horizontal gradient. $S(x) = 1$. Horizontal lines within the SFE are time delays of rays meeting irregularities at E-Layer heights, with the value of β_p marked on each point. Data are taken from ray tracings of Fig. 5.

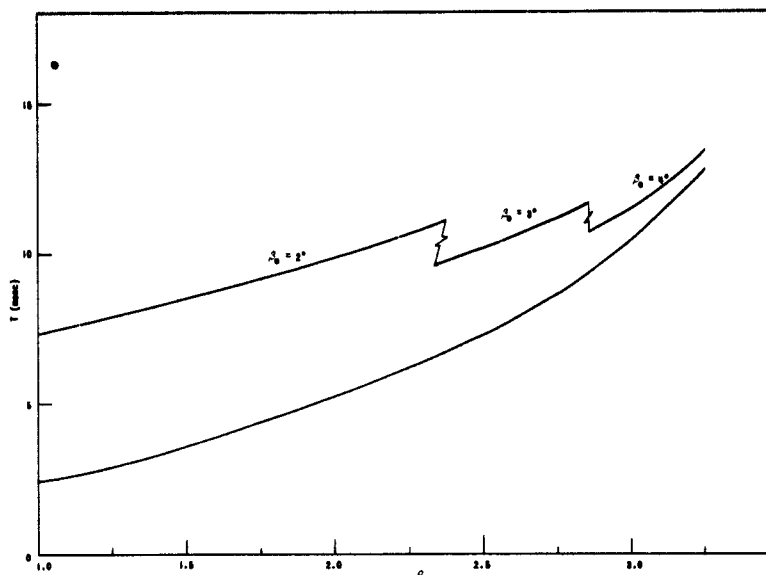


FIG. 13. SHAPE OF SWEEP-FREQUENCY, GROUND-BACKSCATTERED ECHO BOUNDED BY ITS TWO EXTREME TIME DELAYS AS FUNCTIONS OF ρ . β -Chapman layer of $h_{\max} = 300$ km, $H = 100$ km with horizontal gradient, $S(x) = \cos [(x-b)/R]$ with $b/R = 0^\circ$. Time delays correspond to the ray tracings of Fig. 6.

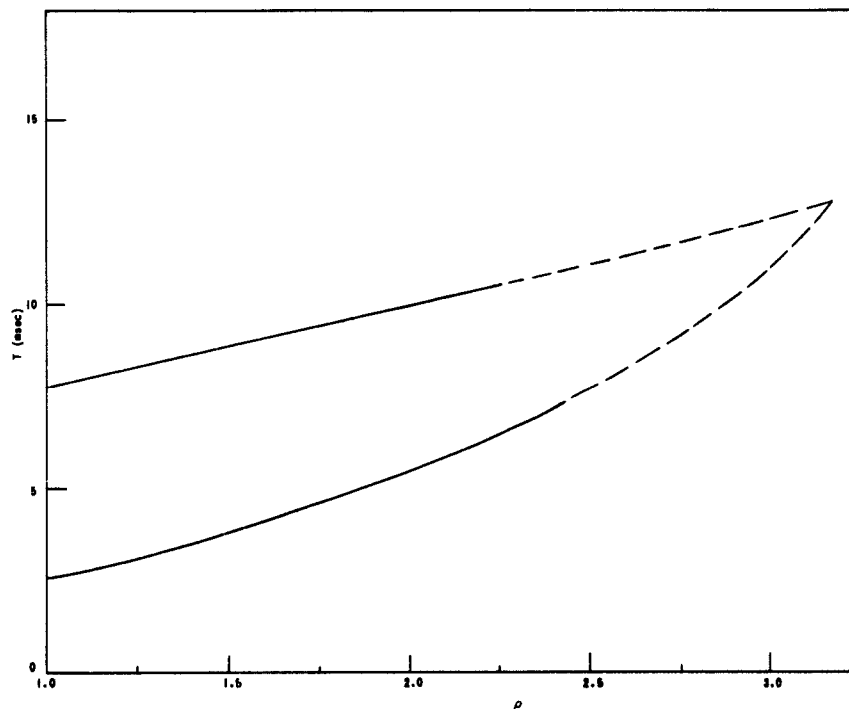


FIG. 14. SHAPE OF SWEEP-FREQUENCY, GROUND-BACKSCATTERED ECHO BOUNDED BY ITS TWO EXTREME TIME DELAYS AS FUNCTIONS OF ρ . β -Chapman layer of $h_{\max} = 300$ km, $H = 100$ km with horizontal gradient, $S(x) = \cos [(x-b)/R]$ with $b/R = +30^\circ$. Time delays correspond to the ray tracings of Fig. 7.

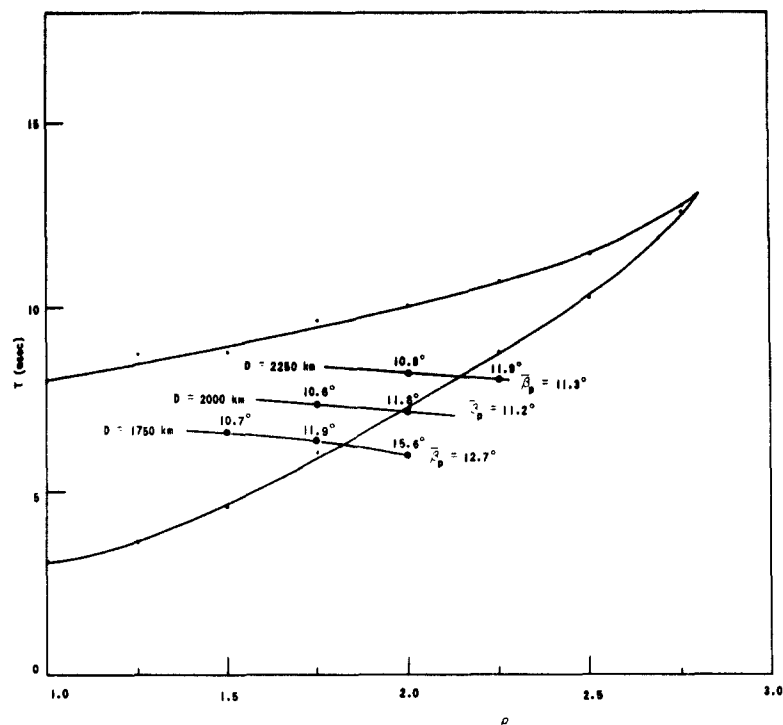


FIG. 15. SHAPE OF SWEEP-FREQUENCY, GROUND-BACKSCATTERED ECHO BOUNDED BY ITS TWO EXTREME TIME DELAYS AS FUNCTIONS OF ρ . β -Chapman layer of $h_{\max} = 300$ km, $H = 100$ km with horizontal gradient, $S(x) = \cos [(x-b)/R]$ with $b/R = +60^\circ$. Time delays correspond to the ray tracings of Fig. 8.

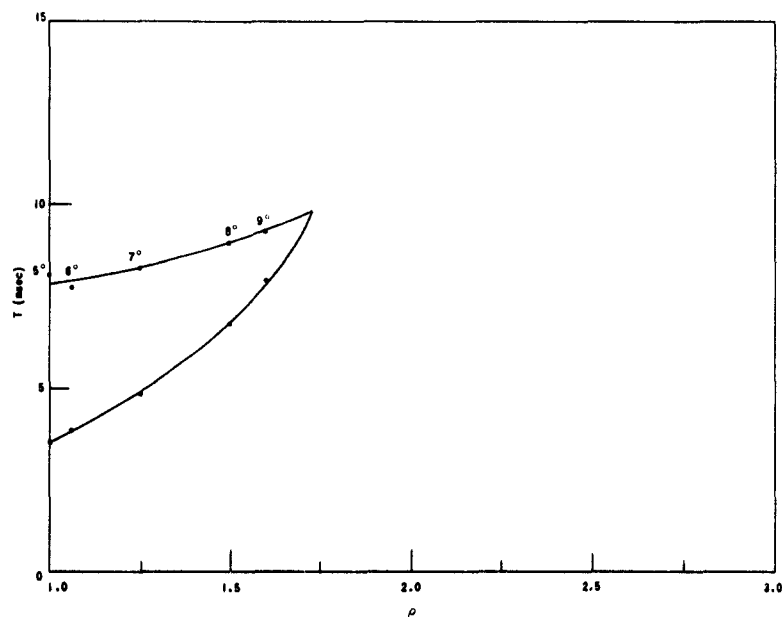


FIG. 16. SHAPE OF SWEEP-FREQUENCY, GROUND-BACKSCATTERED ECHO BOUNDED BY ITS TWO EXTREME TIME DELAYS AS FUNCTIONS OF ρ . β -Chapman layer of $h_{\max} = 300$ km, $H = 100$ km with horizontal gradient, $S(x) = \cos [(x-b)/R]$ with $b/R = -60^\circ$. Time delays correspond to the ray tracings of Fig. 9.

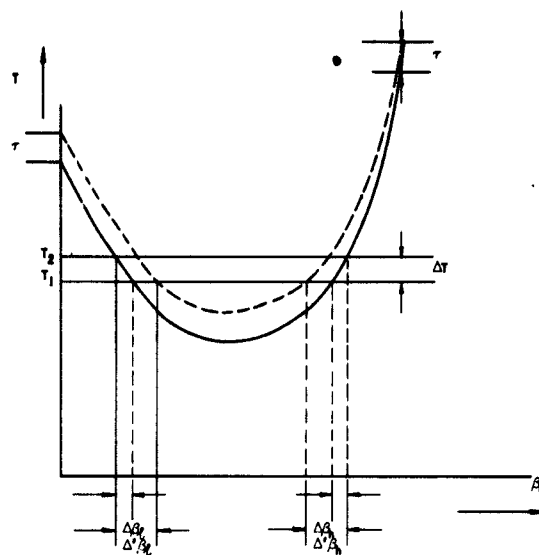


FIG. 17. DETERMINATION OF THE BACK-SCATTER ECHO DELAY PATTERN (TYPE A) FROM THE T VS β_0 CURVE OF FIG. 10.

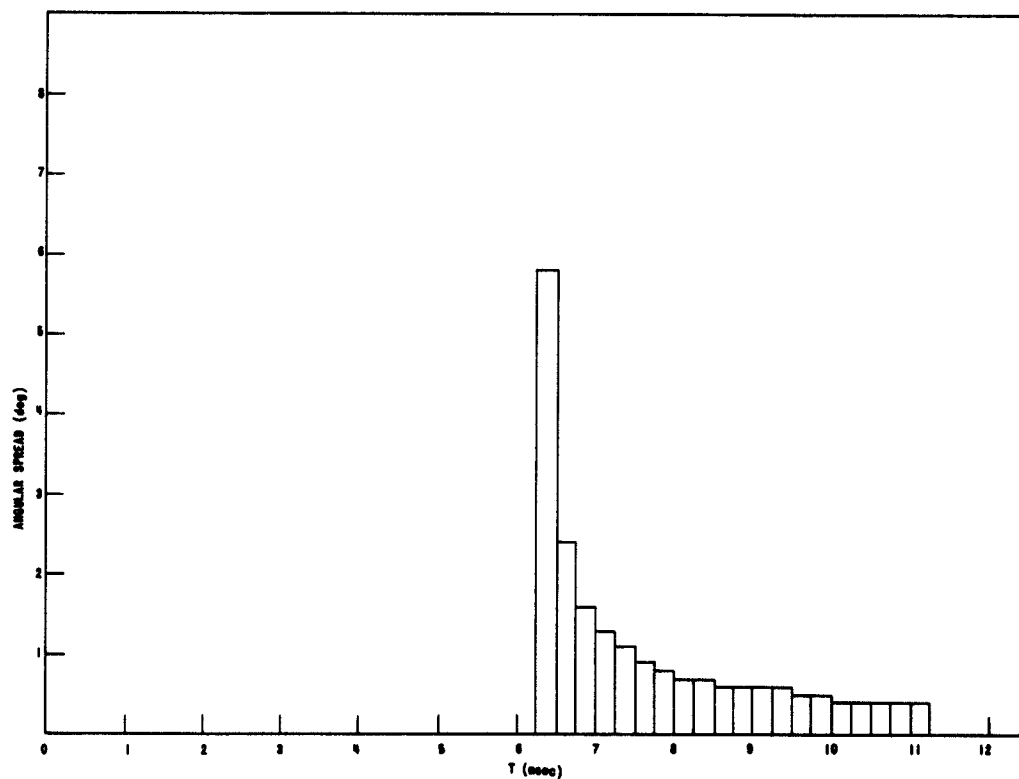


FIG. 18. TYPE A BACKSCATTER ECHO PATTERN (RANGE-AMPLITUDE) DERIVED FROM THE CONSTRUCTION OF FIG. 17. β -CHAPMAN LAYER $h_{max} = 300$ km, $H = 100$ km WITH NO HORIZONTAL GRADIENT OF ELECTRON DENSITY.

In practice, the intensity distribution will be influenced by the antenna's vertical pattern, resulting in the convolution of the two distributions. For low-angle propagation, such as that employed in the present work, the effect will be enhancement of the trailing part of the echo.

Further enhancement will be effected by the finiteness of the pulse duration. This can be seen by referring again to Fig. 17, where the dotted curve is drawn with constant separation equal to the pulse width τ , from the original $T - \beta_0$ curve. In this case the angular spread for a ΔT interval will be that indicated by $\Delta'\beta_l$ and $\Delta'\beta_h$, being the total projection of the two curves on the β_0 axis for that interval.

E. ANALYSIS OF FACTORS AFFECTING SHAPE OF BACKSCATTER ECHO

In this section the effects of the various parameters of the transmission circuit on the shape of the ground-backscatter echo are analyzed to gain insight into the mechanics of the various shapes commonly observed. Attention is limited to the SFE bounded by the two extreme rays of the minimum-time delay and of zero angle. The latter, which forms the upper boundary, is not insignificant because of the effect of the antenna pattern, particularly at higher frequencies, as mentioned earlier.

It is seen in all the curves shown (Figs. 11-16) that, because of the curvature of the earth and the ionosphere, the minimum time delay, particularly in the region of the MUF, no longer bears the simple linear relationship with frequency as under flat-earth conditions (see Eq. 22 below). This is confirmed in many of the records taken with the sounder (Sec. III).

The ionospheric model assumed has a great bearing on the shape of the SFE. In the two electron-height distributions taken--parabolic and the β -Chapman--the difference is most noticeable in the upper boundary corresponding to low-angle rays. Compare Figs. 4 and 12 and observe the flatness of the former as compared with that of the β -Chapman layer. This behavior is to be expected, as the two types of distribution are quite different at the bottom of the layer. The constants for the parabolic distribution used in the determination of Fig. 19 were admittedly

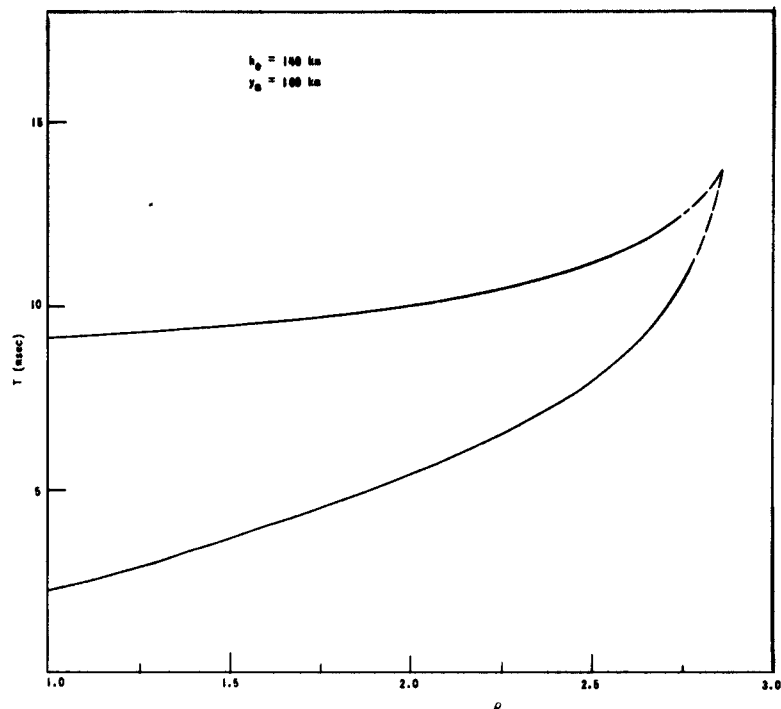


FIG. 19. SHAPE OF THE GROUND-BACKSCATTERED ECHO, BOUNDED BY ITS TWO EXTREME TIME DELAYS (CORRESPONDING TO MINIMUM TIME DELAY AND TANGENT RAYS) AS FUNCTIONS OF THE NORMALIZED FREQUENCY ρ . PARABOLIC LAYER $h_0 = 140$ km, $y_m = 160$ km.

rather nonrealistic, but were chosen for a best fit to the Chapman distribution adopted for the ray tracing. See the three distributions in Fig. 20 drawn for the same maximum ion density, i.e., 10^6 electrons/cm³ at 300-km height.

Comparing the SFE patterns resulting from the two parabolic distributions, the effect of the layer thickness is, as to be expected, to increase the delay spread of the SFE. Hence a thin layer, such as the E or E_s, will return a narrow sweep-frequency echo. Similarly, any stratification or splitting in the ion distribution of the layer would be expected to appear as separate, narrow sweep-frequency echo. See for example the striations in Fig. 21 A-2 at 21.40, Fig. 21 B-2 at 04.20, and Fig. 21 B-4 at 02.20 GMT.

The layer thickness also affects, to a certain extent, the slope of the minimum-time-delay part of the echo as a function of ρ as can be

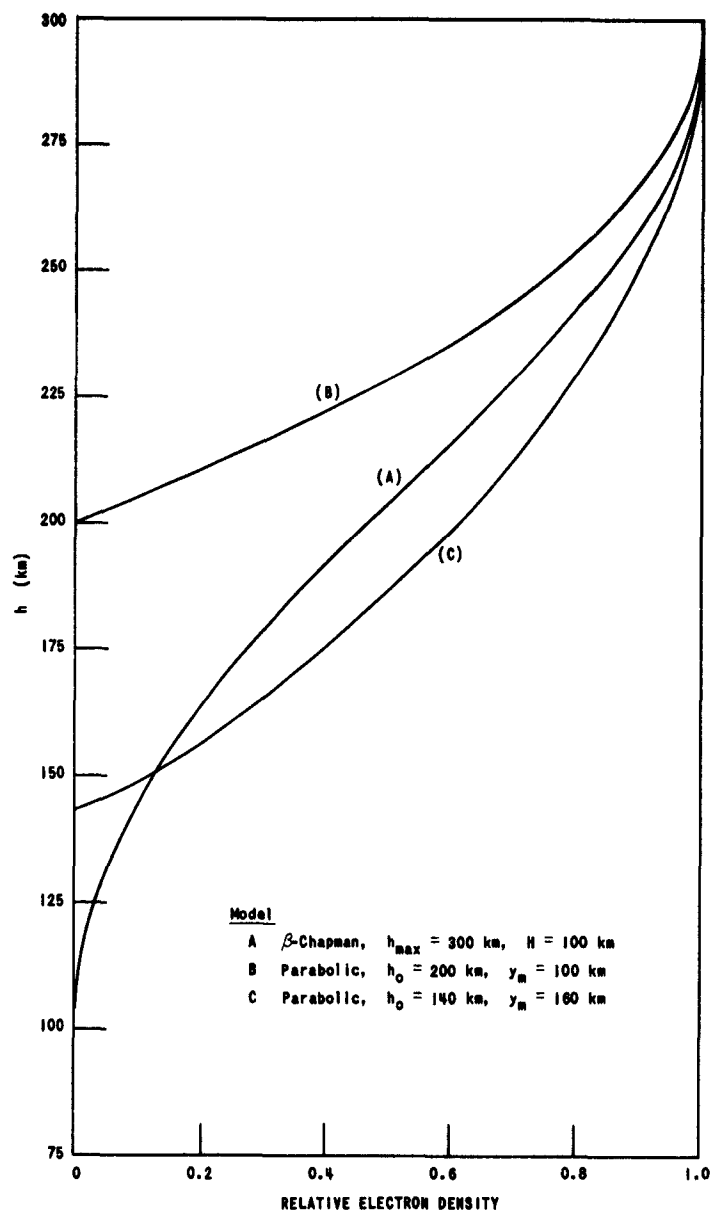
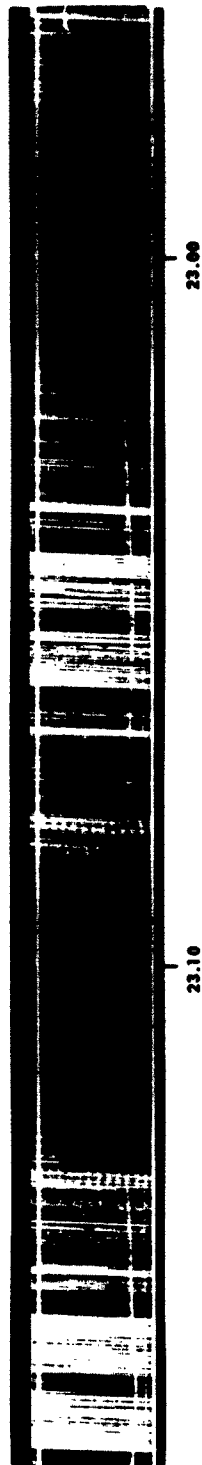
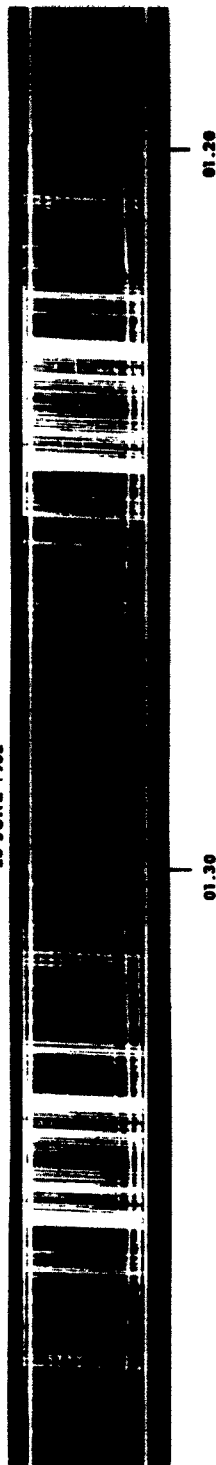


FIG. 20. PLOTS OF ELECTRON DENSITY VERTICAL DISTRIBUTIONS USED IN THE CALCULATIONS. DENSITY SCALE IS RELATIVE TO 10^6 ELECTRONS/cc.

23 JUNE 1962



23 JUNE 1962



23 JUNE 1962

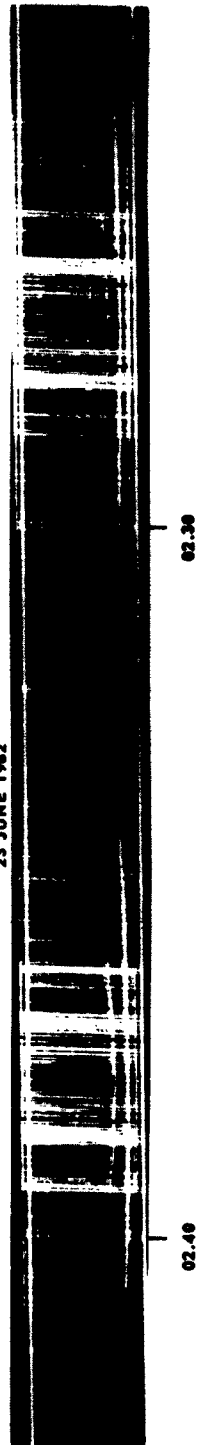
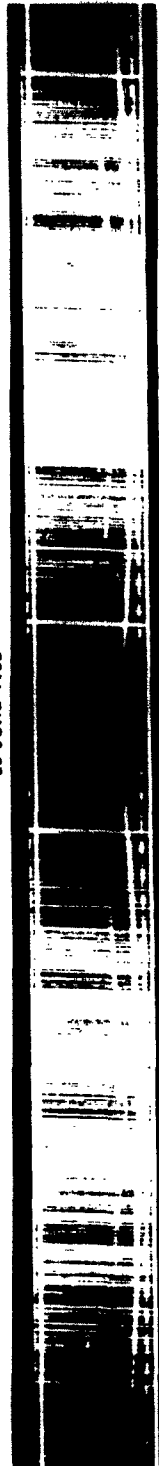


FIG. 21 A-1

23 JUNE 1962



03.20

03.10

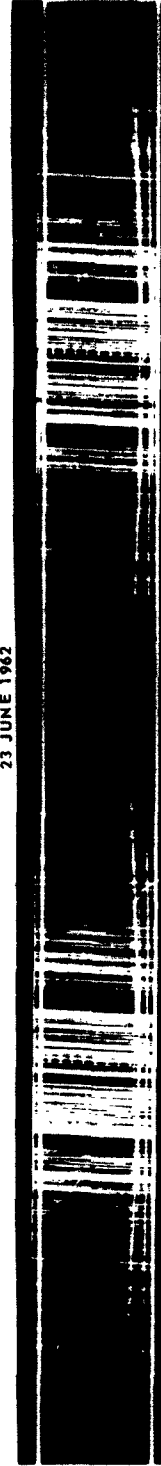
23 JUNE 1962



21.20

21.10

23 JUNE 1962



21.40

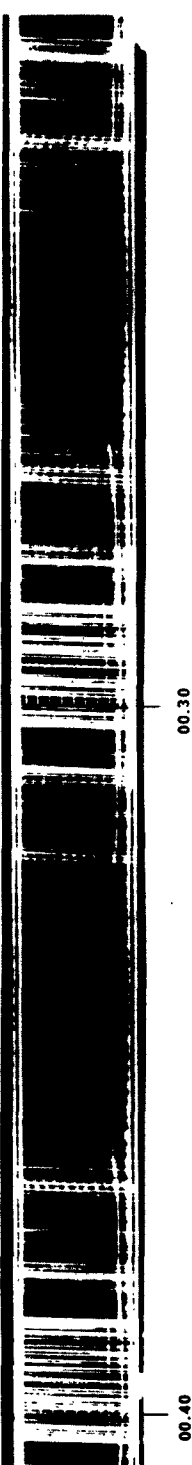
21.30

FIG. 21 A-2

23 JUNE 1962



24 JUNE 1962



24 JUNE 1962

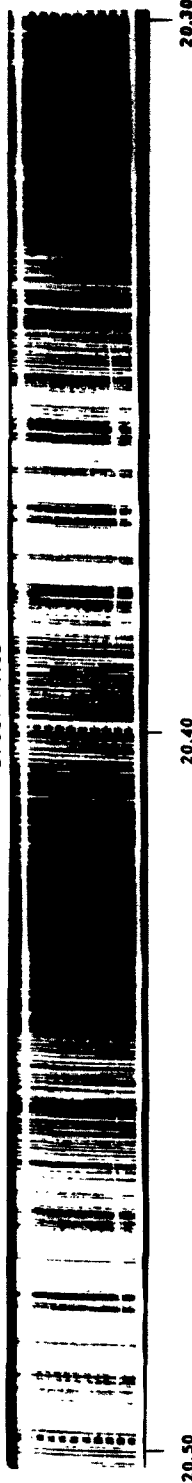


FIG. 21 A-3

Part A-1, -2, -3. Eastward propagation from Stanford during the period 22 - 25 June 1962. Time, in G.M.T., progresses from right to left.

SEL-63-011

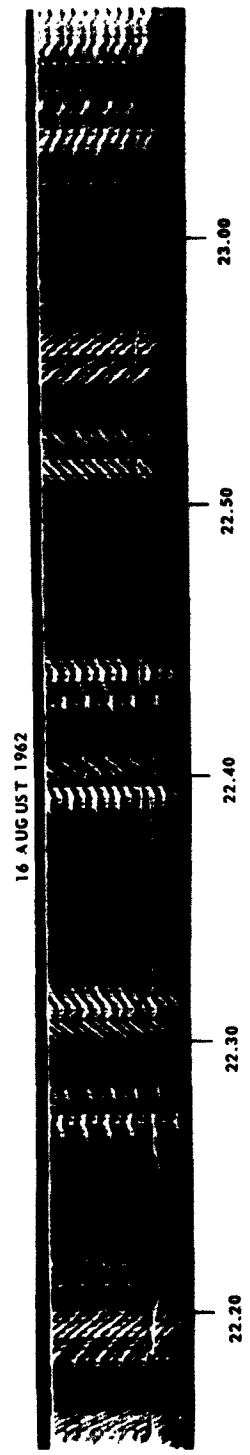
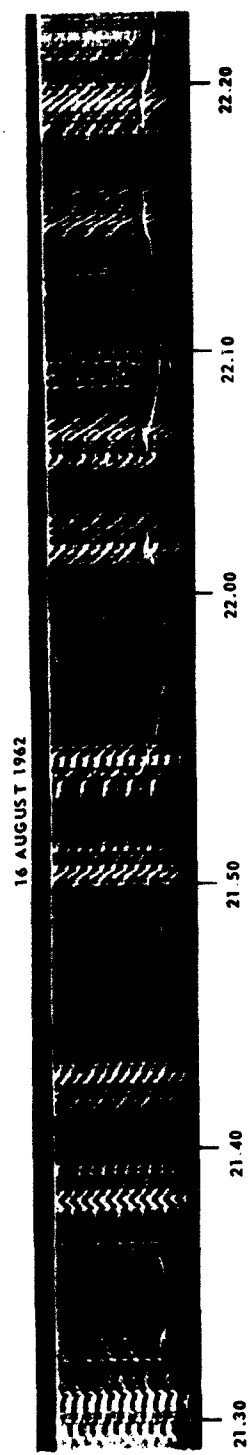
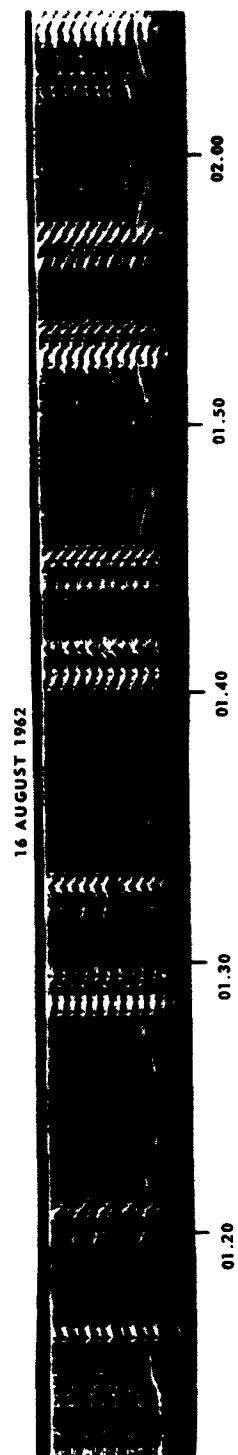


FIG. 21 B-1

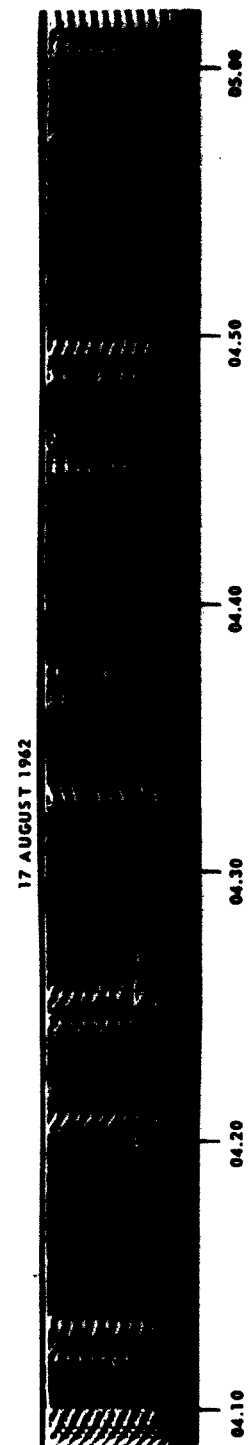
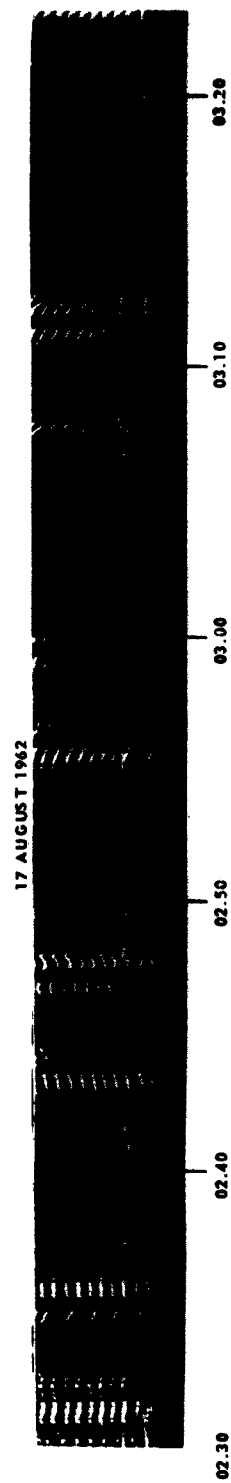
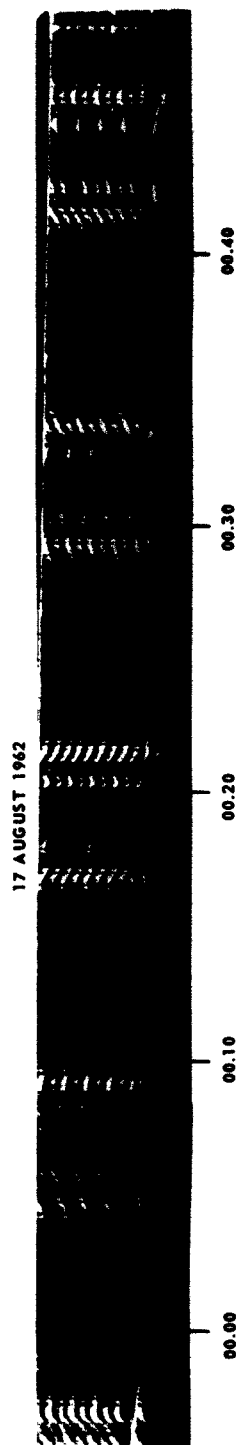


FIG. 21 B-2

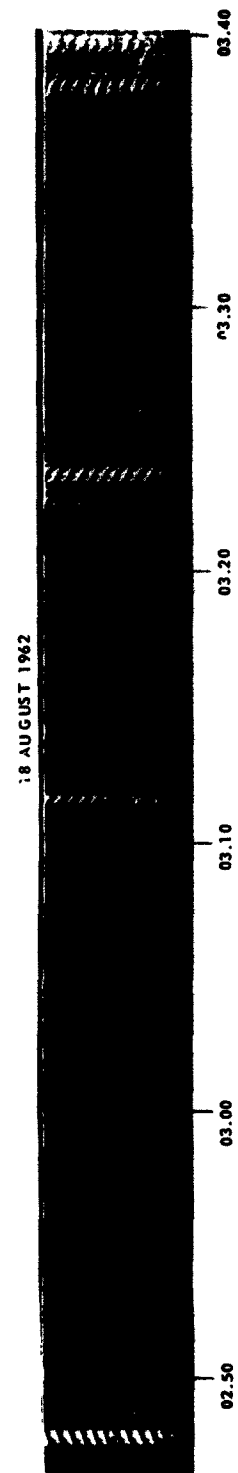
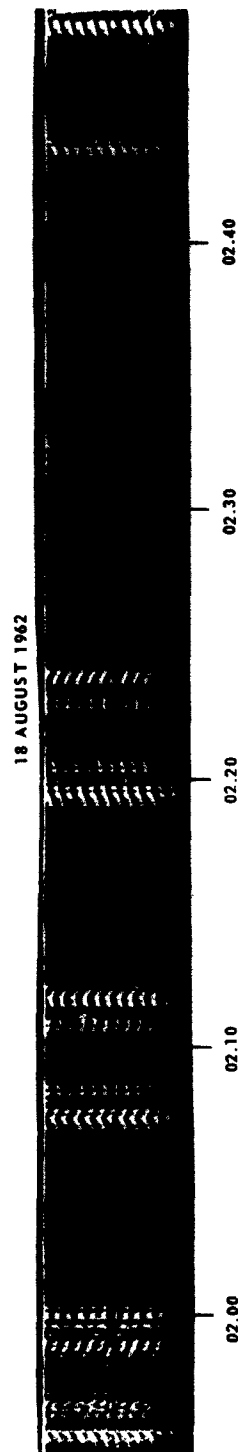


FIG. 21 B-3

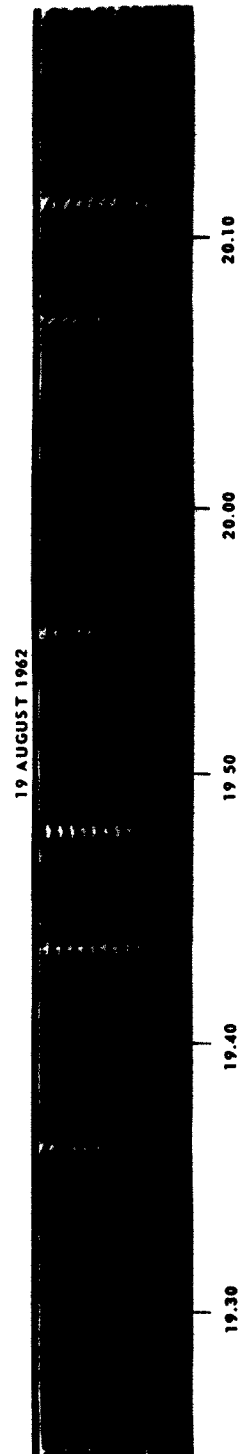
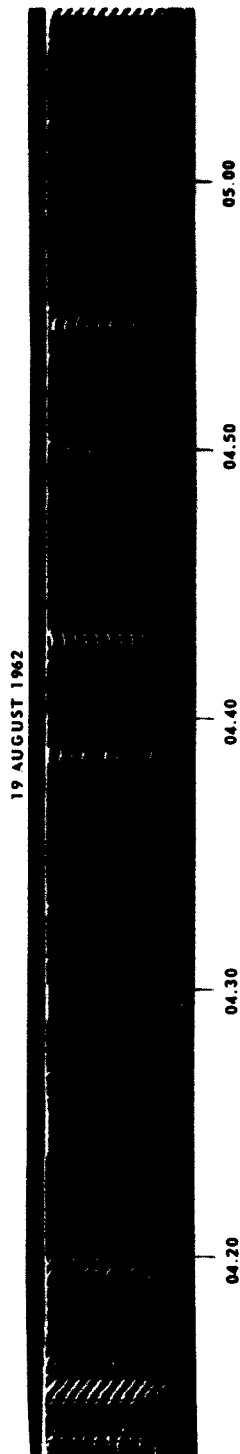
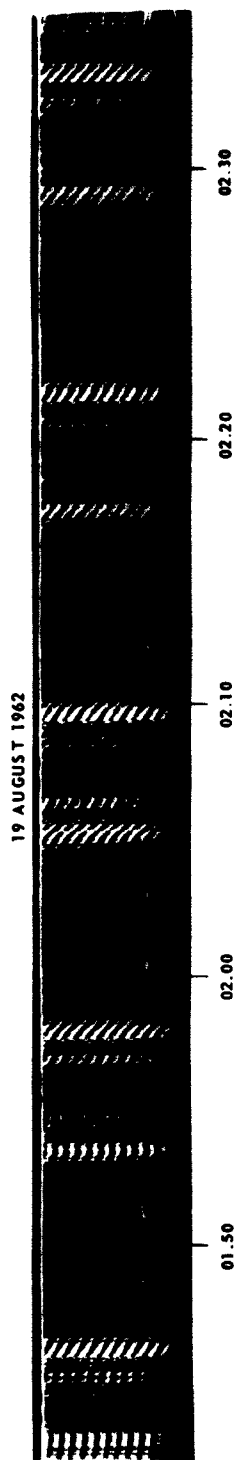


FIG. 21 B-4

Part B-1, -2, -3, -4. Westward propagation from Stamford during the period 16 - 19 August 1962. Time, in G.M.T., progresses from left to right.

FIG. 21. SAMPLES OF CONTINUOUS-SWEEP-FREQUENCY RECORDINGS SHOWING VARIOUS TYPES OF ECHOES.

noted from the following Eq. (22) [Ref. 4] for flat-earth geometry and a parabolic distribution in the layer,

$$P'_{\min} = \left(2 h_v^* \sqrt{1 + \frac{y_m}{h_o}} \right) \rho, \quad (22)$$

where h_v^* is the virtual reflection height corresponding to frequency $f_c / \sqrt{1 + y_m/h_o}$ at vertical incidence. If this value of h_v^* , as obtained from the parabolic-layer expression of Eq. (A.8) in Appendix A, is substituted in Eq. (22) and all the distances are normalized with respect to the layer height h_o , we obtain the following general expression for the normalized oblique distance of minimum-time delay,

$$\frac{P'_{\min}}{h_o} = \left\{ 2 \left[\sqrt{1 + \frac{y_m}{h_o}} + \frac{y_m}{h_o} \coth^{-1} \sqrt{1 + \frac{y_m}{h_o}} \right] \right\} \rho \quad (23A)$$

$$= S \rho \quad (23B)$$

from which the aforementioned slope S can be evaluated in terms of a normalized layer thickness y_m/h_o . It will be seen that the variation of this slope S with the parameter y_m/h_o is relatively slow (S varies from 2.00 to 4.59 as (y_m/h_o) increases from zero to 1.0). Thus, when one considers any particular SFE within a given frequency range, the slope of the leading edge of the pattern is seen to be governed principally by the prevailing critical frequency f_c of the propagation-supporting layer and the height h_o of that layer.

Next, the effect of the horizontal variation of the electron density is to be considered. As mentioned earlier, a cosine function was chosen to take account of the effect of the sun's varying position in the sky, relative to the ray along the path. Figures 13 through 16 show the envelope of the SFE at different positions of the subsolar point along the path. Comparison of Fig. 13, for the condition of noon at the transmitter, with that of Fig. 12, indicating absence of horizontal gradients, shows that the ray corresponding to minimum-time delay is, again, virtually unaffected by the gradient over the path involved. The

presence of a negative electron-density gradient, however, causes some of the low-angle rays to escape reflection at the ground, producing the well-known layer tilt and making an overall shorter echo duration. This effect is further augmented when the subsolar point is located behind the transmitter, as shown in Fig. 16, resulting in shorter frequency range, since the critical frequency for the remaining higher-angle rays will be lower. When the layer tilt is in the opposite direction, the subsolar point being ahead of the transmitter, the slope of the SFE at the P'_{\min} side is mostly affected. In both cases, however, the differences become appreciable at positions of the sun close to sunset and sunrise.

III. SOUNDING EXPERIMENTS

The ground-backscatter sounding was carried out by means of a novel type of sweep-frequency ionosonde suggested by O. G. Villard, Jr., and built by Applied Technology, Inc., around a Hamarlund SP-600 receiver, which acts as a sensitive receiver as well as the frequency-determining element. The detailed design and circuit features are given in an unpublished report. Figure 22 is a block diagram of the transmitting and receiving portions of the equipment when only the exciter part of the transmitter is used, giving a peak output of about 1 kw. Higher-power outputs (approximately 10 kw) are obtained by cascading the "final amplifier" of the exciter to a "power amplifier." Both of these amplifiers are L-C tunable between 14 and 27 Mc/s, and the tuning is made to follow the master frequency automatically by means of servo-motors. A special transmit-receive (T-R) arrangement is used for the employment of a single antenna for both transmission and reception.

The master frequency ($f_o - f_x$) is derived from the local oscillator of the receiver (continuous frequency f_o) by a weak capacitive coupling. After passing through an isolation amplifier, the signal is mixed at the oscillator-mixer with a fixed frequency (f_x) of 3.955 Mc/s (being equal to the receiver first i-f) generated by a crystal oscillator. The mixture component ($f_o - f_x$) is then fed back to the receiver at its rf input side, which is also the input for received signals coming through the T-R switch and the preamplifier, and is tapped off the rf output through an adjacent isolation amplifier and passed to the driver section of the transmitter. Both sections of the transmitter, as well as the oscillator-mixer, are held at cut-off in their normal states and are gated for operation by the pulser during the transmission period. The same gating operation turns off the receiving preamplifier.

Frequency variation is effected by rotating the tuning knob of the receiver. Continuous upward and downward frequency sweeps were made by coupling to a reversible 5-rpm motor controlled by an automatic switching mechanism which is actuated by two microswitches attached to appropriate points on the rotatable tuning scale. The frequency sweep was between 15 and 24 Mc/s during a period of approximately 5 min. in each direction.

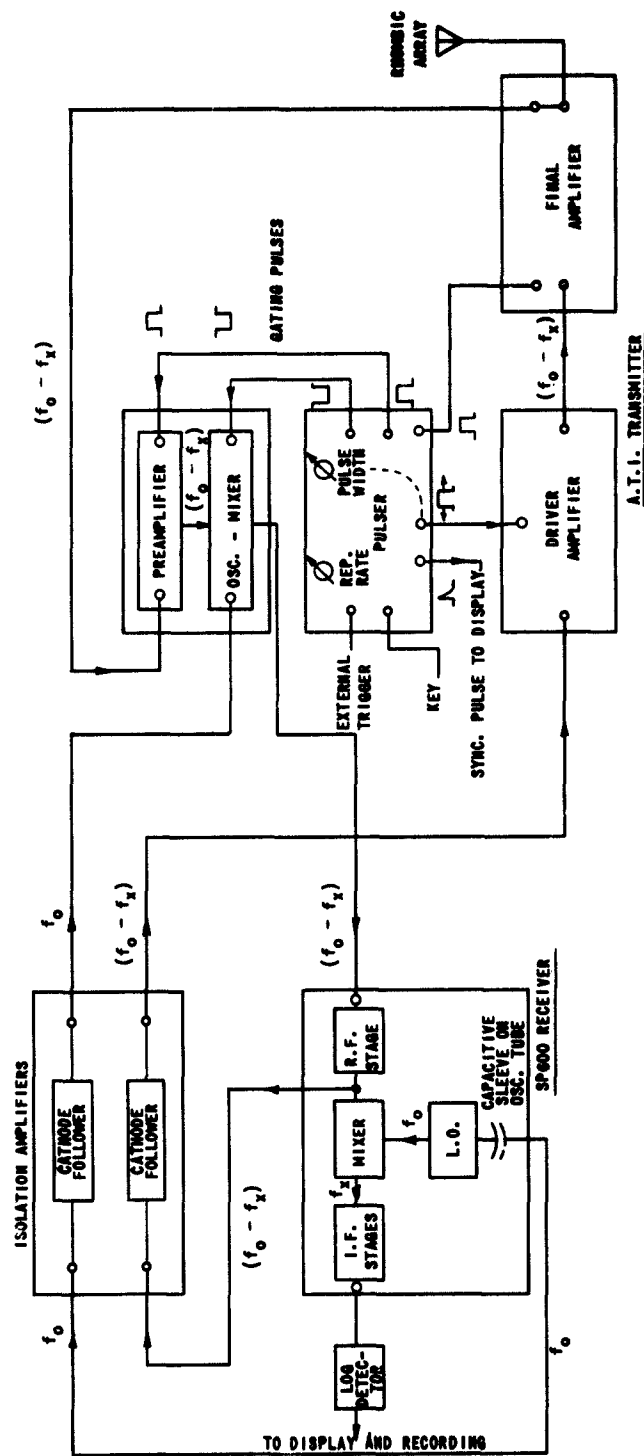


FIG. 22. SIGNAL FLOW AND CONNECTION DIAGRAM OF THE EXCITER-SOUNDER.
 f_o is the frequency of the local oscillator in the "Receiver," and f_x is that of the crystal oscillator in the "Oscillator-Preamplifier" and is 3.955 Mc/s.

Because of the continuous sweep of the frequency, the receiver would be slightly detuned with respect to the returning echo, and this effect would progressively increase with increasing echo delay, making multi-hop reception more difficult. The purpose of the slow sweep was to reduce this effect. In addition, the receiver bandwidth was increased at the expense of slightly more interference.

As in most conventional sounders, the received SFE was monitored by an A-scope and recorded directly on a moving photographic film from a second oscilloscope whose beam was intensity-modulated by the signal. Thus its time-base deflection was at right angles to the direction of film travel.

The width of the transmitted pulse used was 1 msec. The records do not show this directly, as it is masked by the 3-msec gate impressed on the receiver. A delay of 0.75 msec takes place before the generation of the rf pulse. The PRF was about 10 pps.

At 10-min intervals, a narrow train of 1500-km (1 msec) range marks is superimposed on the received signal. Both the transmitter pulses and this train are triggered from the same source.

The antenna system, which is used for both transmission and reception, is a broadside array of eight rhombics, which can be made to fire in either the east or the west direction by appropriate switching. Full details of the antennas are to be found in Refs. 8 and 9, but the following is a summary of the main characteristics:

Height above ground	18.9 meters
Leg length	112 meters
Apex angle	75 deg
Horizontal beam width	2 deg
Vertical beam width	8 deg
Elevation angle of main lobe	from 8.2 deg at 25.6 Mc/s to 14 deg at 15.0 Mc/s

Some of the records taken are shown in Fig. 21.

IV. DISCUSSION OF DATA

A. GENERAL

The sweep-frequency ground-backscatter records, continuously obtained for the frequency range of 15 - 25 Mc/s, show, on the whole, the characteristic shape of the SFE derived by means of ray tracing in Chapter II. This shape applies both to the first and to the multi-hop echoes.

Note that the presentation of the SFE as bounded by the two extreme rays does not by itself provide information as to the relative intensity of the various echo returns, which, as seen from Fig. 18, diminishes rapidly at the trailing portion of the echo. Thus, details of this portion are sometimes lost and the upper boundary of the SFE will not be seen. The use of a logarithmic detector in the receiver helped a great deal in bringing out these details.

The presence of irregularities and departure from the assumed electron-density profile present additional features to the echo pattern, appearing mostly as striations along the sweep. These are intensifications of certain portions of the SFE at apparently random time delays. Most of the records appearing in Fig. 21 were chosen to show these striations.

Two main types of steady, regular striations can be identified in relation to the variation of their mean time delay with frequency: 1) frequency-dependent striations and 2) frequency-independent striations. Examples of type 1) are shown in Fig. 21 B-2 around 03.00 GMT and of type 2) in Figs. 21 A-3 at 20.40, 21 B-1 at 21.50 and 21 B-3 at 01.50 GMT.

The frequency-dependent striations are mostly of the regular type which follow a positive variation with frequency. There are some, however, such as those shown in Figs. 21 A-2 at 21.40, 21 B-1 at 22.40 and 21 B-2 at 04.30 GMT which exhibit a slight negative slope. For reasons that will be explained in the next section, this category of echoes might be more closely associated with type 2), which shows clear frequency independence.

The distinction between types 1) and 2) becomes less obvious when the striation appears at the trailing edge of the SFE, since this portion of the main echo is formed by the low-angle-ray returns, which are

themselves less frequency-dependent in their time delay than those at the opposite, leading edge, corresponding to minimum-time delay (see, for example, Fig. 4). As mentioned before, this is the result of the limiting effect caused by the curvature of the earth and the ionosphere. Examples of these limit echoes are seen in Table 1.

TABLE 1. EXAMPLES OF LIMIT ECHOES

East		West	
Limit Echoes	Hours	Limit Echoes	Hours
22 June	2300	17 August	0030
23 June	0230	17 August	0430
23 June	2210	18 August	0200
24 June	2030	19 August	0150

The intensification of the SFE at various slant ranges corresponding to their equivalent-time delays can be the result of either 1) time-delay focusing; or 2) improvement in the reflection coefficient at the points of incidence of the ray along its path.

Both vertical and horizontal gradients in ion-density distribution would result, at suitable angles and frequencies and with correct signs, in some degree of time-delay focusing. The former gives rise to the minimum time-delay focusing appropriate to a layer with given thickness and ionization. The same mechanism can be assumed to be responsible for multiple intensification beyond the leading edge of the SFE if the propagation-supporting ionosphere happens to be stratified or consisting of small layers, separated perhaps by small ledges along the profile, each contributing its own minimum time delay. The variation with frequency of each of them would be as discussed in Sec. II.A and governed by Eq. (22). The horizontal gradients, on the other hand, will result in corrugation or ripple in the effective reflecting surface of the ionosphere, which, as postulated by Tveten [Ref. 10], Hofmann [Ref. 11] and others, can produce a certain degree of focusing in the rays.

Reflection enhancement can take place along the ray path by the presence of highly ionized irregularities in the F or E layer, or

large objects on the ground, such as mountain ranges [Refs. 12, 13]. Such irregularities undoubtedly produce echoes that vary very little with frequency, and their relevance to the experimental results is discussed in more detail in the next section.

B. CONSTANT-RANGE ECHOES

1. General

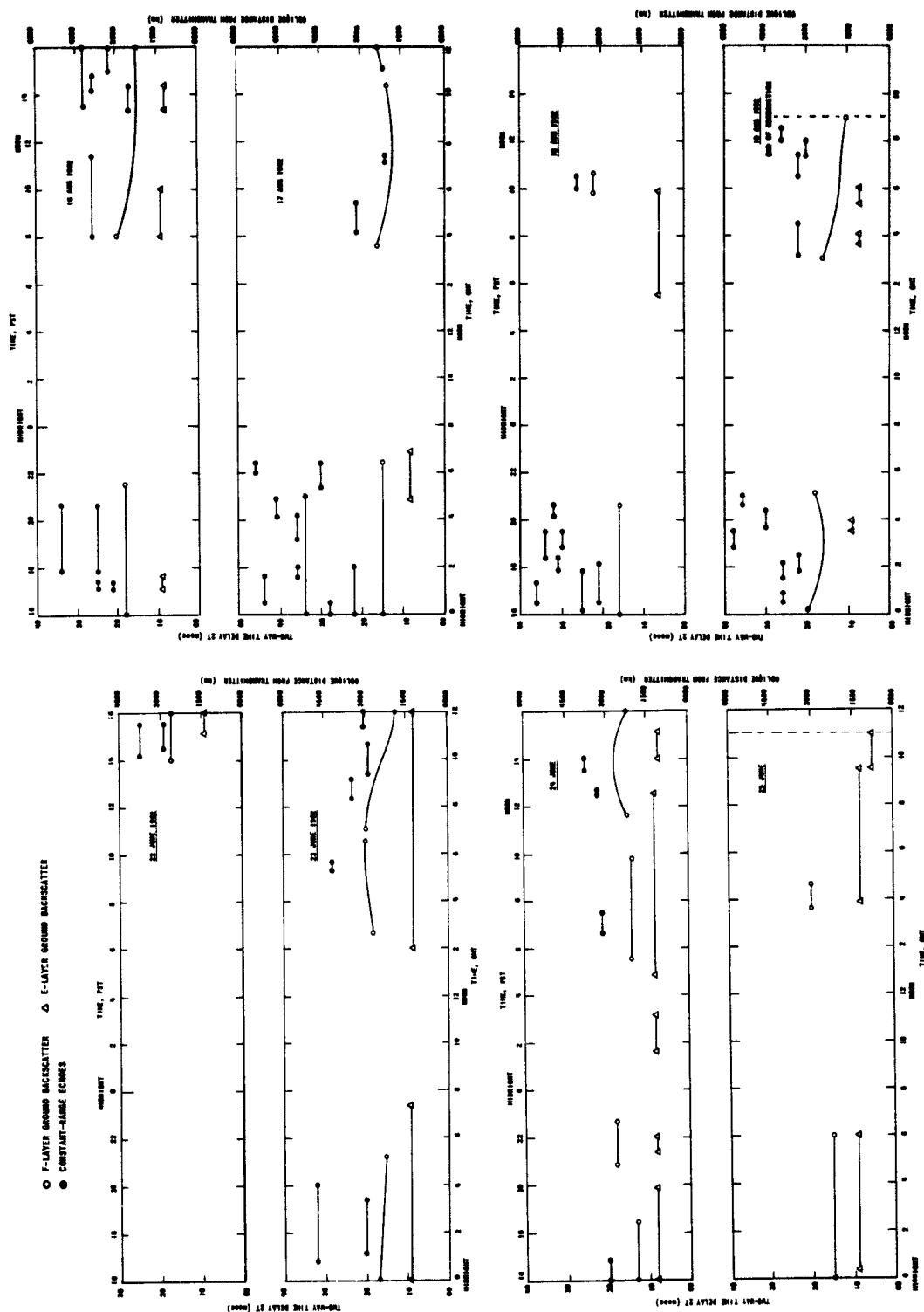
This type of echo has been observed in this laboratory for some time [Ref. 4]. These echoes give rise to frequency-independent striations (type 2), which, as discussed in the previous section, represent echo intensification presumably resulting from irregularities of finite dimensions located in the ray path.

These striations are observed in association with an F-layer-propagated echo. Figure 23 shows a plot of the time and duration of occurrence vs time delays of such echoes, extracted from the continuous recordings of oblique soundings in the eastward and westward directions during June and August, 1962, respectively. It is seen that the lifetime of these echoes is between a few minutes and an hour or two. Longer-duration echoes can also be seen in the plot but are, in reality, trains of shorter-duration, usually occurring at close intervals at approximately the same slant ranges. It will thus not be accurate to deduce a statistical mean of echo lifetime based on Fig. 23.

No detectable motion in these echoes is observed in the records, especially motion that would result in a change of the striation position with respect to the SFE.

2. Ground Objects and F-Layer Irregularities

Examination of the slant ranges involved in the present F-layer-propagated backscatter does not reveal any definite or consistent ground irregularity that might be taken as a source of constant-range reflection. The possibility does exist, however, that the cluster of echoes observed around 3000 km in the eastward direction might be emanating from the Florida coastline, while the Pacific islands may be responsible for the more numerous western echoes, particularly from the Hawaii region (4000 - 5000 km in the direction of the rays). However, it is difficult to



a. F-layer and E-layer ground backscatter (Eastward).

b. F-layer and E-layer ground backscatter (Westward).

FIG. 23. OCCURRENCE OF CONSTANT-RANGE ECHOES.

explain the relatively short and sporadic appearance of the echoes on that basis.

Though of little significance to the case of oblique transmissions, analysis of the regular vertical-incidence ionograms taken by the C-2 sounder at Stanford shows, for the same periods, absence of any echoes that might originate from some ion-concentration irregularities in the F layer overhead.

The effect of a reflecting irregularity in the F layer can be followed in any of the ray tracings presented above, although the actual time delay cannot be obtained accurately since the computed time delays have only been integrated over the full path of the ray. (An approximation was made for the E-layer backscattering by subtracting the delay in the 100-km-high, non-deviative portion from the total delay. See Sec. IV.A.3.) However, two features of the echoes that would be obtained can be deduced from a study of the ray tracings:

1. The time delay of such echoes would be fairly independent of frequency, though they would exhibit a slight negative slope, which would generally be less than that for the E-layer backscattering.
2. The constant-range echoes thus produced would invariably extend well beyond the edge formed by the minimum-time-delay portion of the SFE, since some reflection from the irregularity can conceivably occur within the skip zone. The amount of extension would depend on the relative location of the irregularity in the F layer and on its ionization intensity. Such appreciable protrusions are not observed in the recordings.

The foregoing discussion regarding the F layer is based on the assumption that the reflecting irregularities are of such high local electron densities that they will possess sharp gradients and thus produce forward scattering. F-layer irregularities of milder gradients would allow at least partial penetration of the rays, thereby suffering retardation, and would therefore exhibit frequency dependence in their time delay.

The vertical-incidence ionograms which were examined also show approximately equal sporadic-E activity overhead during the two periods, yet the backscatter sounding shows definite preponderance of E-layer echoes at about 1000 km when the observation was directed inland

(Fig. 23.A). This increase may well be a reflection from the Rocky Mountain range [Ref. 15]. On the other hand, the following may be an alternative cause of these close-range echoes.

3. Irregularities in the E Layer

Peterson et al [Ref. 16] and Gallagher [Ref. 17] observed field-aligned irregularities in the E region (centered around the geomagnetic north from Stanford), which produced strong, but rapidly fading, direct-backscatter echoes resulting from the incidence of the radar wave on the elongated ionization at right angles to its long axis of symmetry. These middle-latitude irregularities may be associated with extensions of the polar or equatorial type of sporadic-E to middle latitudes. The slant range at which this phenomenon has been observed around Stanford, in the absence of ionospheric bending, depends on the direction of propagation, and ranges from about 200 km due magnetic north (declination 17.5°E) to more than 1000 km on either side of this direction. This phenomenon certainly cannot account for all of the constant-range echoes observed in the present experiments, some of which extend beyond 6000 km, but one can picture a ray meeting the axis of the irregularity orthogonally at the E-layer level after being reflected by the upper F layer. With this geometry, and Stanford as center, it is possible to meet the geomagnetic-field lines at right angles for distances extending beyond 8000 km. It is shown in Appendix D that normal intersection with a field line F of positive dip angle I takes place when the vertical or elevation angle β_p (with respect to the horizontal) of the downcoming ray satisfies the following simple relation:

$$\tan \beta_p = \cos (180 - \alpha) \cot I, \quad (23)$$

with α being the angle between the two meridian planes containing the ray and the geomagnetic field line at the point of intersection P. If the directions of these planes relative to the magnetic north are A and D (declination) respectively, the angle α will be:

$$\text{for westward propagation, } \alpha = 180 - (A - D). \quad (24)$$

$$\text{for eastward propagation, } \alpha = 180 - (A + D). \quad (25)$$

With values* of I and α corresponding to points P along the two directions of propagation, a plot is presented in Fig. 24 giving the necessary value of β_p at these points to satisfy the perpendicularity condition. The negative values of β_p to the east indicate that the ray meets the line of force in its upward direction.

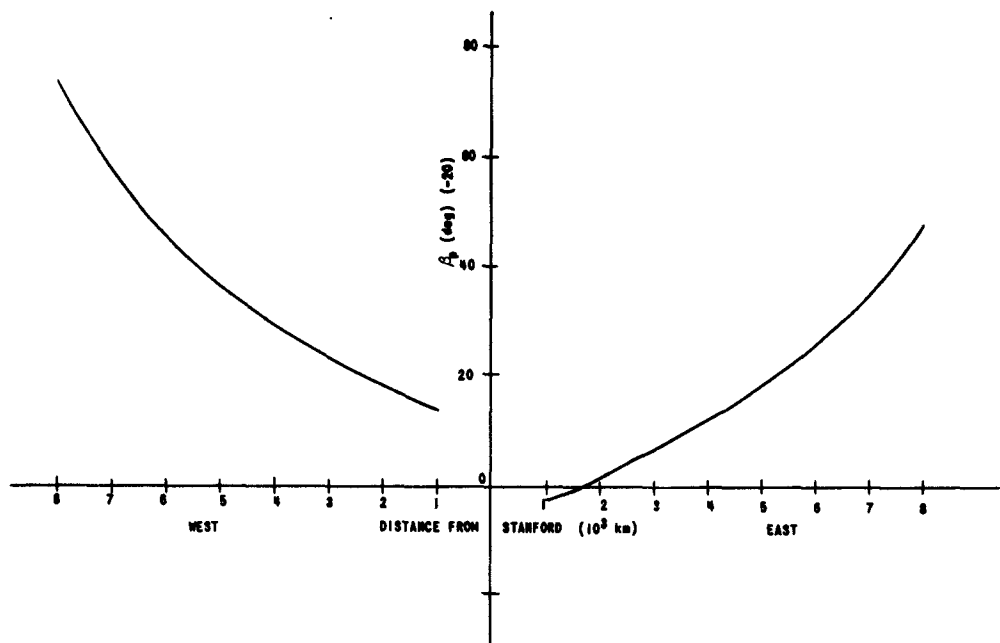


FIG. 24. PLOT OF VERTICAL ANGLES β_p AT WHICH DOWNCOMING RAYS MEET GEOMAGNETIC FIELD LINES ORTHOGONALLY IN THE E LAYER AT VARIOUS DISTANCES DUE EAST AND DUE WEST OF STANFORD.

It will be noticed from Fig. 24 that, under this assumption of meeting the irregularities in a downcoming direction of the ray, the westward propagation requires appreciably larger values of the angle β_p to achieve perpendicular intersection. Inspection of the rays traced for a layer in the absence of a horizontal gradient (Fig. 5) shows that the angle of the downcoming ray meeting an irregularity at a height of 100 km at a given range does not vary materially from 10 deg. The horizontal lines shown embedded in the SFE pattern of Fig. 12 are one-way time delays calculated from these tracings between the transmitter

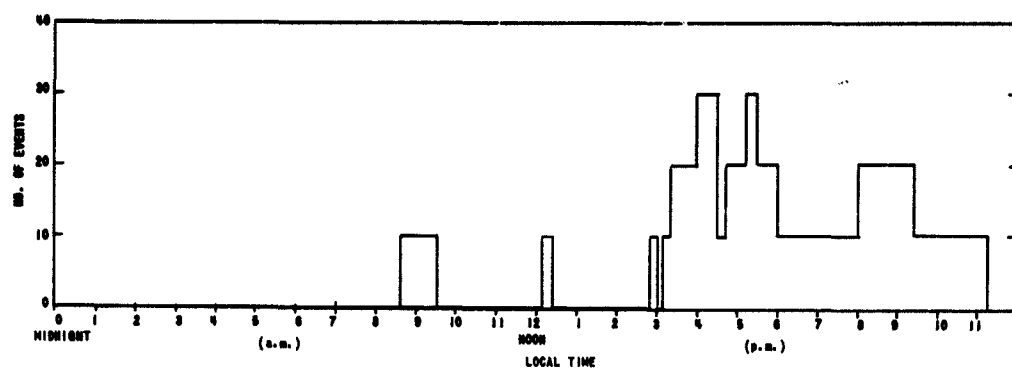
* Calculated from the data provided by the geomagnetic maps in [Ref. 18]. Values at E-layer height are considered to be approximately the same as those given for ground level.

and points P distant 1750, 2000, and 2250 km, respectively, from it and at 100-km height. The values of $\bar{\beta}_p$ shown are average β_p of all the rays that strike each particular point P at that height.

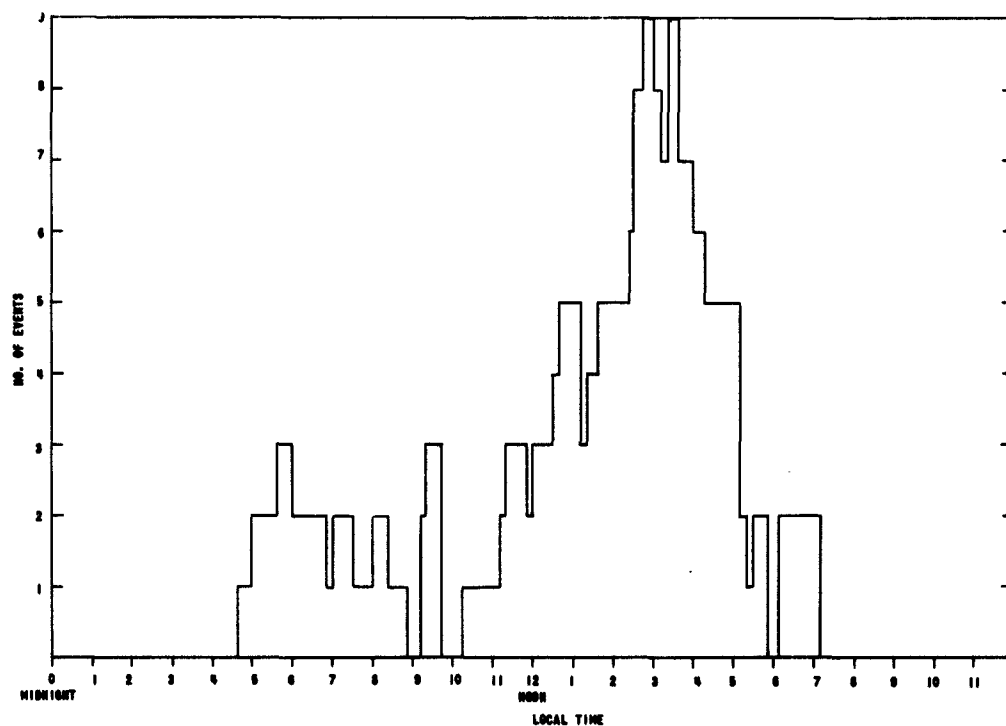
Thus, it is seen that, although the time delays of the rays striking the irregularity at the point P remain fairly constant, particularly at the more distant points, the average value of the required angle β_p appears to be too high for the easterly direction of propagation and too low for the opposite direction.

Possibly one way of reconciling these discrepancies is to consider the time of appearance of these constant-range echoes on a local basis, as shown in the histograms of Fig. 25. It is found that the mean of this time is about the same in either direction, with a tendency towards the early afternoon for the westward propagation and towards the late afternoon for the eastward propagation. This approximately constant mean time of appearance in the afternoon indicates that the horizontal gradients of the ion densities in the F layer are of opposite signs in the two directions, resulting in layer tilts, the senses of which do tally with the inequality of β_p for given ranges in these directions (Fig. 24). However, the layer tilts produced by the cosine gradient assumed for the SFE of Fig. 15, which corresponds to the westerly direction, does not seem to bring about a substantial increase in the angle β_p (the mean values are also shown for each ground range).

There are two features of the constant-range echoes that the ray tracings have brought out, under the above assumption of the E-layer origin of the backscattering irregularities. These are 1) their slight negative slope, diminishing rapidly at longer ranges; and 2) their extension slightly beyond the minimum-time-delay boundary (by an amount equivalent, for any given frequency, to the oblique distance of the irregularity from the ground-reflection point which the intercepted ray would have reached). Both of these characteristics are observed in varying degrees in many of the echoes found in the recordings, as can be seen, for example, in Figs. 21 B-2 at 04.50 and 21 B-4 at 01.50 GMT, though many others do not exhibit these features but still appear frequency independent.



a. Eastward Propagation.



b. Westward Propagation.

FIG. 25. STATISTICAL PLOT OF THE FREQUENCY OF OCCURRENCE OF CONSTANT RANGE ECHOES AGAINST TIME OF OCCURRENCE PREVAILING LOCALLY AT THE POSITION OF THE IRREGULARITY.

V. CONCLUSIONS AND RECOMMENDATIONS

The ray analysis has shown that the shape of the SFE pattern (delay time vs frequency) derived from either of the two methods discussed in Sections II.C and II.D, respectively, agrees well with that observed in normal sweep-frequency sounding. From a study of the shape, certain properties of the propagation-supporting ionosphere can be surmised, such as layer thickness and the presence of extensive horizontal gradients.

It has further been shown, and graphically demonstrated by an extension of Peterson's construction to curved-earth geometry, that the tangent ray makes a definite contribution at the trailing edge of the above pattern, and varies least with frequency, approaching frequency independence between wide limits. This is noteworthy in respect to the constant-range striations with which this study has been chiefly concerned. The study of the two types of striations appearing within the SFE, classified with respect to the variation of their time delay with frequency, has revealed that those which vary positively are the result of echo-delay focusing produced by suitable vertical or horizontal gradients in the ionosphere. On the other hand, highly reflective irregularities (such as sharp gradients) whether midway along the path of the ray (in the F region) or at its far end (in the E region or the ground) can produce echoes whose delay times are fairly independent of the frequency.

As far as the latter type of echo is concerned, analysis of the backscatter data collected for the two directions of propagation has shown that, of the three possibilities, the E-layer origin of the expected irregularities is the most likely. It is also quite feasible that these irregularities are in line with the geomagnetic field, although, for the layer model adopted, some kind of layer tilt must be invoked if the maximum-reflection condition is to be fulfilled. Their predominantly daytime appearance seems, a priori, to dissociate such echoes from the nocturnal type observed by Gallagher [Ref. 17] in the same layer, but this finding is far from being conclusive because of the short period of observation of the constant-range echoes in the

present study, during a great part of which night propagation via the F layer was absent.

Frequency-sweep sounding has brought to light certain types of irregularities that would not be distinguishable in normal fixed-frequency backscatter sounding, nor ordinarily in multifrequency operation. Further investigation needs to be carried out to establish their morphology and azimuthal extent, and to find out more about their location and apparent motion.

APPENDIX A. DERIVATION OF THE EQUIVALENT GROUP PATH AS A FUNCTION OF THE TAKE-OFF ANGLE FOR CURVED GEOMETRY

1. In Terms of Virtual Height

Fig. 1, the sine law for the triangle OAB gives:

$$\begin{aligned} P' &= 2(R + h') \frac{\sin \theta}{\cos \beta_o} \\ &= 2(R + h') \frac{\cos (\beta_o + \phi_o)}{\cos \beta_o} \end{aligned} \quad (A.1)$$

and since

$$\cos (\beta_o + \phi_o) = \cos \beta_o \cos \phi_o - \sin \beta_o \sin \phi_o,$$

then

$$P' = 2(R + h') (\cos \phi_o - \tan \beta_o \sin \phi_o). \quad (A.2)$$

Again, from the sine law for the triangle OAB, and letting $r = R/(R + h')$, we get

$$\sin \phi_o = r \cos \beta_o \quad (A.3)$$

and

$$\tan \beta_o \sin \phi_o = r \sin \beta_o \quad (A.4)$$

Also

$$\begin{aligned} \cos \phi_o &= (1 - \sin^2 \phi_o)^{1/2} \\ &= (1 - r^2 \cos^2 \beta_o)^{1/2}. \end{aligned} \quad (A.5)$$

From (A.2), (A.4) and (A.5), we get

$$P' = 2(R + h') [(1 - r^2 \cos^2 \beta_o)^{1/2} - r \sin \beta_o] \quad (A.6)$$

or

$$P' = 2 \{ [(R + h')^2 - R^2 \cos^2 \beta_o]^{1/2} - R \sin \beta_o \}. \quad (A.7)$$

2. In Terms of Layer Parameters

If a parabolic distribution of electron density is assumed for the layer, then for vertical incidence of a wave at frequency f_v

$$h' = h_o + \frac{1}{2} y_m (f_v/f_c) \ln \left[\frac{1 + (f_v/f_c)}{1 - (f_v/f_c)} \right] \quad (\text{A.8})$$

where: h_o = height of the bottom of the layer

y_m = half thickness of the layer

f_c = plasma frequency or critical frequency at vertical incidence

At oblique incidence, and when the effect of the curvature of the ionosphere at the point of "reflection" of the wave of frequency f_{ob} is neglected,

$$f_v = f_{ob} \cos \theta_o. \quad (\text{A.9})$$

When

$$\rho = (f_{ob}/f_c)$$

$$\frac{f_v}{f_c} = \rho \cos \theta_o \quad (\text{A.10})$$

and, from Eq. (A.5),

$$\frac{f_v}{f_c} = \rho [1 - r^2 \cos^2 \theta_o]^{1/2}. \quad (\text{A.11})$$

When the above is put in Eq. (A.8) and is expressed in terms of $(R + h')$:

$$(R + h') = (R + h_o) + \frac{1}{2} y_m \rho (1 - r^2 \cos^2 \theta_o)^{\frac{1}{2}} \ln \left[\frac{1 + \rho (1 - r^2 \cos^2 \theta_o)^{\frac{1}{2}}}{1 - \rho (1 - r^2 \cos^2 \theta_o)^{\frac{1}{2}}} \right].$$

(A.12)

Remembering that r is a function of $(R + h')$, we evaluate the latter by successive approximations using a digital computer.

3. Rate of Variation

Putting $R_1 = (R + h')$ in Eq. (A.7) and differentiating with respect to β_0 we obtain

$$\begin{aligned} \frac{dP'}{d\beta_0} &= 2 \left[\frac{1}{2} (R_1^2 - R^2 \cos^2 \beta_0)^{-\frac{1}{2}} \left(2R_1 \frac{dR_1}{d\beta_0} + 2R^2 \sin \beta_0 \cos \beta_0 \right) - R \cos \beta_0 \right] \\ &= 2 \left[\left(R_1 \frac{dR_1}{d\beta_0} + R^2 \sin \beta_0 \cos \beta_0 \right) (R_1^2 - R^2 \cos^2 \beta_0)^{-\frac{1}{2}} - R \cos \beta_0 \right] \end{aligned} \quad (A.13)$$

For tangential propagation $\beta_0 \approx 0$, hence

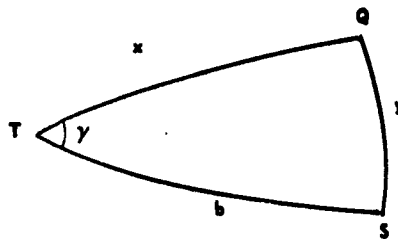
$$\begin{aligned} \frac{dP'}{d\beta_0} &\approx 2 \left[R_1 \frac{dR_1}{d\beta_0} (R_1^2 - R^2)^{-\frac{1}{2}} - R \right] \\ &= 2 \left[\frac{(R_1 - R)(R_1 + R)}{R_1^2} \right]^{-\frac{1}{2}} \frac{dR_1}{d\beta_0} - 2R \end{aligned} \quad (A.14)$$

Eq. (A.14) can further be approximated by putting $(R_1 + R) \approx 2R$; we then obtain

$$\frac{dP'}{d\beta_0} \approx \left(\frac{2R}{h'} \right)^{\frac{1}{2}} \frac{dh'}{d\beta_0} - 2R \quad (A.15)$$

At low values of β_0 the virtual height h' tends to be constant, and the first term of (A.15) becomes negligible. Therefore $dP'/d\beta_0 \rightarrow (-2R)$ as $\beta_0 \rightarrow 0$.

APPENDIX B. GEOMETRY OF TRANSMISSION PATH WITH RESPECT TO SUN'S ZENITH ANGLE



In the above sketch, T represents the transmitter and Q the projection on the earth's surface of a point q in the ray path. S is the subsolar point, and b, x, and y are distances on the surface of the earth (of radius R). The sun's zenith angle is therefore given by:

$$\chi = (y/R) \quad (\text{B.1a})$$

and

$$\cos \chi = \cos (y/R) \quad (\text{B.1b})$$

From spherical trigonometry

$$\cos \frac{y}{R} = \cos \frac{x}{R} \cos \frac{b}{R} + \sin \frac{x}{R} \sin \frac{b}{R} \cos \gamma \quad (\text{B.2})$$

Two limiting cases are considered:

1. The subsolar point along the x direction, i.e., in the plane of the ray path, $\gamma = 0$,

$$\cos (y/R) = \cos (x/R) \cos (b/R) + \sin (x/R) \sin (b/R)$$

$$\cos \chi = \cos [(x/R) - (b/R)] \quad (\text{B.3})$$

2. The subsolar point in a meridian plane orthogonal to that of the ray path $\gamma = \pi/2$

$$\cos \chi = \cos (x/R) \cdot \cos (b/R) \quad (\text{B.4})$$

APPENDIX C. DERIVATION OF ECHO GROUP TIME DELAY

In the ray tracings of Fig. 5 et seq., which are plotted in terms of the ground distance x (from the transmitter) and the true height h , the length of a elemental portion of the traced curve is

$$ds = [(dx)^2 + (dh)^2]^{\frac{1}{2}} \quad (C.1)$$

Hence

$$\frac{ds}{dx} = \left[1 + \left(\frac{dh}{dx} \right)^2 \right]^{\frac{1}{2}} \quad (C.2)$$

However, although the tracings give the coordinates of any point in the ray path in terms of x and h correctly, the Cartesian system does not yield the true shape or the true length of the ray path, which follows the curvature of the earth. With this approximation in mind, the group delay is derived from the ray equation as follows:

Let t = time elapse in pulse propagation

T = total delay of pulse for one hop and one way

v_g = group velocity of wave

μ = phase refractive index

μ' = group refractive index

c = wave velocity in free space

Then

$$dt = ds/v_g = (\mu'/c) ds \quad (C.3)$$

Under the ionospheric conditions assumed in this work, the effect of the earth's magnetic field and of collisional damping can be neglected, so that:

$$\mu = 1/\mu' \quad (C.4)$$

and

$$\begin{aligned} dt &= (1/c\mu) ds \\ &= (1/c\mu)(ds/dx) dx. \end{aligned} \quad (C.5)$$

Hence

$$T = \frac{1}{c} \int_{\text{path}} \left[\frac{1 + (dh/dx)^2}{\mu^2} \right]^{\frac{1}{2}} dx \quad (\text{C.6})$$

From Eq. (14) in the text,

$$T = \frac{1}{c} \int_{x=0}^{h=0} \left[\frac{1 + (dh/dx)^2}{1 - F(h) \cdot S(x)/\rho^2} \right]^{\frac{1}{2}} dx \quad (\text{C.7})$$

The terms in Eq. (C.7) are tapped off the ray-tracing program.

APPENDIX D. DETERMINATION OF THE ANGLE OF THE DOWNCOMING RAY MEETING A GEOMAGNETIC FIELD LINE AT RIGHT ANGLES

In Fig. 26, which is drawn for westward propagation, in the plane of the paper, let P be the point of intersection of the ray CP in this meridian plane with the geomagnetic field line F contained in another meridian plane making an angle α with the former. In the present work, the location of P is at a height of 100 km. Also, let β and I be the angles which the two vectors make with the horizontal at P.

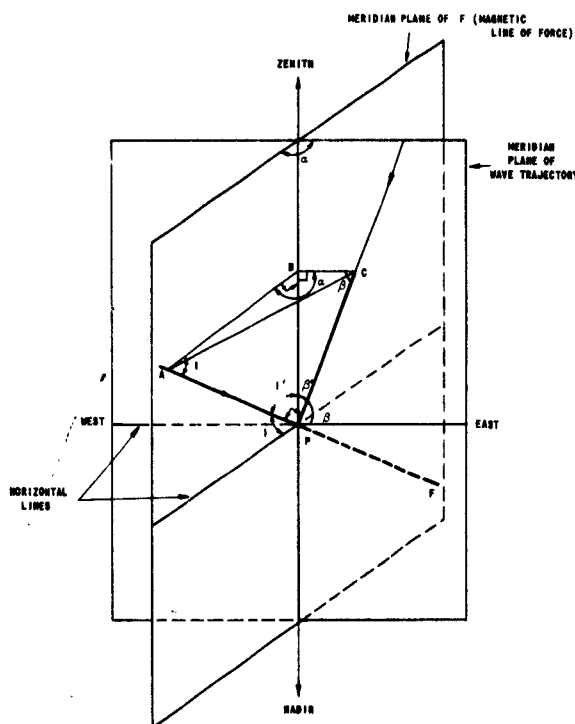


FIG. 26. GEOMETRY OF THE NORMAL INTERSECTION OF A DOWNCOMING RAY WITH A GEOMAGNETIC FIELD LINE LOOKING WEST OF STANFORD.

In a plane cutting the two aforementioned meridians orthogonally, a triangle ABC is formed from its intersection with the ray and the magnetic field, with angle ABC equal to α , so that

$$\overline{AC}^2 = \overline{AB}^2 + \overline{BC}^2 - 2 \overline{AB} \overline{BC} \cos \alpha. \quad (D.1)$$

In the two right-angled triangles with P as the common apex

$$\overline{AB} = \overline{PA} \cos I \quad (D.2)$$

and

$$\overline{BC} = \overline{PC} \cos \beta. \quad (D.3)$$

Combining the above three equations

$$\overline{AC}^2 = \overline{PA}^2 \cos^2 I + \overline{PC}^2 \cos^2 \beta - 2 \overline{PA} \cdot \overline{PC} \cos \alpha \cos \beta \cos I. \quad (D.4)$$

Also in triangle APC

$$\overline{AC}^2 = \overline{PA}^2 + \overline{PC}^2. \quad (D.5)$$

Equating (D.4) and (D.5) and rearranging, we get

$$\overline{PA}^2 \sin^2 I + \overline{PC}^2 \sin^2 \beta = - 2 \overline{PA} \cdot \overline{PC} \cos \alpha \cos \beta \cos I. \quad (D.6)$$

Again, in the two right-angled triangles having PB as the common side,

$$\overline{PB} = \overline{PC} \sin \beta = \overline{PA} \sin I. \quad (D.7)$$

From (D.6) and (D.7) we obtain the relationship

$$\tan \beta = - \cos \alpha \cot I. \quad (D.8)$$

REFERENCES

1. D. Nielson et al, "An Investigation of the Backscatter of High-Frequency Radio Waves from Land, Sea Water and Ice," Stanford Research Institute Report, Project 2909, Contract Nonr 2917(00), May 1960.
2. O. G. Villard, Jr., and A. M. Peterson, "Scatter Sounding: A Technique for Study of the Ionosphere at a Distance," Trans. IRE, A-P, 3, 1952, pp. 186-201.
3. N. Smith, "The Relation of Radio Skywave Transmission to Ionosphere Measurements," Proc. IRE, 27, 1939, pp. 332-347.
4. A. M. Peterson, "The Mechanism of F-Layer Propagated Backscatter Echoes," J. Geophys. Res., 56, 1951, pp. 221-237.
5. P. Lejay and D. Lepechinsky, "Field Intensity at the Receiver as a Function of Distance," Nature, 165, 1950, p. 306.
6. M. S. Wong, "Ionospheric Ray Tracing with Analog Computer," Paper presented at the International Conference on Electromagnetic Wave Propagation, Liege, Belgium, 6 Oct 1958.
7. J. A. Ratcliffe, Physics of the Upper Atmosphere, Academic Press, New York, 1960.
8. G. Barry and O. G. Villard, Jr., "Characteristics of Small-Scale F-Layer Irregularities Deduced from Backscatter Soundings Made with a Steerable Narrow-Beam Antenna," TR No. 22, Contract Nonr 225(33), Stanford Electronics Laboratories, Stanford University, Jan 1961.
9. J. A. Martin, "Design of Rhombic Antenna Array for Stanford University," Antenna Systems Laboratory Internal Report, Stanford Research Institute, Mar 1958.
10. L. H. Tveten, "Ionospheric Motions Observed with High Frequency Backscatter Sounders," J. Res. Nat. Bur. Stds., Sec. D., 65D, 1961, pp. 115-127.
11. T. R. Hofmann, "Some Characteristics of F-Layer Irregularities Deduced from Backscatter Soundings Made with a Slewable Antenna Having a 2° Azimuthal Beamwidth," TR No. 36, Contract Nonr 225(33), Stanford Electronics Laboratories, Stanford University, Jun 1961.
12. R. Silberstein, "A Note on Sweep-Frequency Backscatter Observations," J. Geophys. Res., 59, 1954, p. 138.
13. W. Dleminger, "The Scattering of Radio Waves," Proc. Phys. Soc. (London), 64, 1951, pp. 142-158.

14. L. P. Bolgiano, Jr., "Some Characteristics of Multiple-Hop Sweep-Frequency Backscatter Observations between 15 and 54 Mc/s," TR No. 17, Contract Nonr 225(33), Stanford Electronics Laboratories, Stanford University, Oct 1960.
15. R. D. Egan and A. M. Peterson, "Backscatter Observations of Sporadic E," TR No. 2, NSF Grant Y22-10/309, Stanford Electronics Laboratories, Stanford University, May 1961.
16. A. M. Peterson, et al, "Regularly Observable Aspect-Sensitive Radio Reflections from Ionization Aligned with the Earth's Magnetic Field and Located within the Ionospheric Layers at Middle Latitudes," J. Geophys. Res., 60, 1955, pp. 497-512.
17. P. B. Gallagher, "Analysis of a New Type of Radio Scattering from the Ionospheric E-Region," TR No. 107, Contract N6onr 251(07), Stanford Electronics Laboratories, Stanford University, May 1956.
18. Handbook of Geophysics, U.S.A.F. Geophysics Research Directorate, The Macmillan Co., New York, 1960.

TEPEE DISTRIBUTION LIST

March 1963

Headquarters, Foreign Technology
Div.
Wright-Patterson AFB, Ohio
1 Attn: ID-A3a
1 Attn: ID-ElB
1 Attn: TD-XLA

Headquarters, AF Cambridge
Research Labs
Office of Aerospace Research
USAF, L.G. Hanscom Field
Bedford, Mass.
1 Attn: CRRK Dr. Philip Newman
1 Attn: CRRRI Mr. Wm. F. Ring
1 Attn: Dr. G.J. Gassman

Comm. and AFCRL, OAR, USAF
L.G. Hanscom Field
Bedford, Mass.
1 Attn: T.P. Conley/CRRIP

Comm., Hq., Electr. Syst. Div.
L.G. Hanscom Field
Bedford, Mass.
1 Attn: Harry Byram/ESRUT

Hq., USAF, Office of Assist. Chief
of Staff
Washington 25, D.C.
1 Attn: AFCIN-IC

Hq. U.S. Air Force
Washington 25, D.C.
1 Attn: AFTAC/TD-5

Hq., North American Air Defense
Command
Ent Air Force Base
Colorado Springs, Colo.
1 Attn: NELC - Advanced Projects
Group

Hq., Space Systems Division
Air Force Systems Command
USAF, Air Force Unit Post Office
Los Angeles 45, Calif.
1 Attn: Tech. Lib.

Hq., Rome Air Development Center
AF Systems Command
USAF, Griffiss Air Force Base, N.Y.
1 Attn: RALTT-2-Mr. F.C. Bradley
1 Attn: RAUEL-3-Mr. B. Cooper

Hq., Strategic Air Command
Offut Air Force Base, Neb.
1 Attn: DOCE

Comm., AFSC, RTH
Bolling Air Force Base, Md.
1 Attn: Lt./Col. Richard Cosel

Comm. Officer
U.S. Army Signal Radio Propagation Agency
Ft. Monmouth, N.J.
1 Attn: SIGRP-A

Comm. Officer
U.S. Army Signal Missile Support Agency
White Sands Missile Range, N.M.
1 Attn: SIGWS-PO

Hq., U.S. Army Material Command
Bldg., T-7 -
Washington 25, D.C.
1 Attn: AMCRD-DE-MI

TEPEE 1 (3-63)

Systems Branch
U.S. Army Scientific Liaison
and Advisory Group
Apex Station, Washington 4, D.C.
2 Attn: Mr. Arthur H. Frost

Chief, U.S. Army Security Agency
Arlington Hall Station
Arlington 12, Va.
1 Attn: LADEV-S

Comm. Officer
U.S. Army Signal Electronic
Research Unit
P.O. Box 205
1 Mountain View, Calif.

Comm. Officer
Picatinny Arsenal
Dover, N.J.
1 Attn: Technical Information
Lib.

Institute for Defense Analyses
1710 H St., N.W.
Washington 6, D.C.
1 Attn: Dr. Nils L. Muench

Comm. Officer
Army Rocket & Guided Missile
Agency
U.S. Army Ordnance Missile Comm.
Redstone Arsenal, Ala.
1 Attn: Mr. James E. Norman

Chief of Naval Operation
Dept. of the Navy
Washington 25, D.C.
1 Attn: Op-70
1 Attn: Op-92
1 Attn: Op-922B2
1 Attn: Op-723D
1 Attn: Op-07TE

Chief, Bureau of Ships
Dept. of the Navy
Washington 25, D.C.
1 Attn: Code 362A

Director, Special Projects
Dept. of the Navy
Washington 25, D.C.
1 Attn: SP-2041

Comm. Officer
U.S. Naval Ordnance Test Unit
Patrick Air Force Base, Fla.
1 Attn: N3

Comm., U.S. Naval Missile Center
Pt. Mugu, Calif.
1 Attn: Technical Library
Code N03022

Comm., Naval Air Test Center
Patuxent River, Md.
1 Attn: Weapons Systems Test Div.
(Code 424)

Director, U.S. Naval Research Laboratory
Washington 25, D.C.
1 Attn: Code 5320
1 Attn: Code 2027

Comm. Officer and Director
U.S. Navy Electronics Laboratory
San Diego 52, Calif.
1 Attn: Library

Chief of Naval Research
Dept. of the Navy
Washington 25, D.C.
1 Attn: Code 427
1 Attn: Code 463
1 Attn: Code 402C
5 Attn: Code 418

Commanding Officer
U.S. Naval Ordnance Laboratory
Corona, Calif.
1 Attn: Mr. V.E. Hildebrand
Code 453

Chief, Bureau of Naval Weapons
Dept. of the Navy
1 Washington 25, D.C.

*Armed Services Tech. Information
Agency
Arlington Hall Station
10 Arlington 12, Va.

Director, Weapons Systems
Evaluation Group
Rm. 1E875, The Pentagon
1 Washington 25, D.C.

Institute for Defense Analyses
Washington 6, D.C.
1 Attn: RESD - Dr. Paul von
Handel

Director, Advanced Research
Projects Agency
Washington 25, D.C.
1 Attn: LCDR D. Chandler
1 Attn: Mr. Jack Ruina
1 Attn: Dr. Cabell A. Pearse
1 Attn: Mr. A. Van Every

Director, National Security Agency
Ft. G.G. Meade, Md.
1 Attn: C3/TDL

Director, National Bureau of Standards
Boulder, Colo.
1 Attn: Mr. Richard C. Kirby
(Chf., Radio Systems Div.)
1 Attn: Mr. L.H. Tveten
(HF/VHF Research Section)

Office of the Secretary of Defense
The Pentagon
Washington 25, D.C.
1 Attn: Albert Weinstein/ODDRE
Rm. 3E-1030

ACF Electronics Division
ACF Industries, Inc.
3355 52nd Ave.
Hyattsville, Md.
1 Attn: Mr. Wm. T. Whelan (R & D)
**Inspector of Naval Material
401 Water St.
Baltimore 2, Md.

Aero Geo Astro Corp.
Edsall and Lincoln Rd.
Box 1082, Alexandria Va.
1 Attn: Mr. D. Reiser
**Inspector of Naval Material
401 Water St.
Baltimore 2, Md.

Aero Geo Astro Corp.
13624 Magnolia Ave.
Corona, Calif.
1 Attn: Mr. A. Walters
**Inspector of Naval Material
401 Water St.
Baltimore 2, Md.

Radio Corp. of America
Aerospace Communications &
Control Div.
Burlington, Mass.
1 Attn: Mr. J. Rubinovitz
**Inspector of Naval Material
495 Summer St.
Boston 10, Mass.

Stanford Research Institute
Communications & Prop., Lab.
Menlo Park, Calif.
1 Attn: Mr. R. Leadabrand
Communications & Prop. Lab.
1 Attn: Mr. L.T. Dolphin
**Commanding Officer
Office of Naval Research
Branch Office
1000 Geary St.
San Francisco, Calif.

The University of Michigan
Research Security Office
P.O. Box 622
Ann Arbor, Mich.
1 Attn: Ralph E. Hiatt
Head, Rad. Lab.
**Office of Naval Research
Resident Repr.
Univ. of Mich.
820 E. Washington St.
Ann Arbor, Mich.

The University of Michigan
Institute of Science & Technology
P.O. Box 618, Ann Arbor, Mich.
1 Attn: BAMIRAC-ad
**Office of Naval Research
Resident Repr.
University of Michigan
820 E. Washington St.
Ann Arbor, Mich.

Raytheon Company
Communications and Data Processing Ops.
1415 Boston-Providence Turnpike
Norwood, Mass.
1 Attn: L.C. Edwards
**Resident Naval Inspector of Material
Raytheon Manufacturing Co.
Waltham, Mass.

Mass. Institute of Technology
Radio Physics Division
Lincoln Laboratory
P.O. Box 73
Lexington 73, Mass.
1 Attn: Dr. John V. Harrington
1 Attn: Dr. James H. Chisholm
(Radio Propagation Group)
1 Attn: Mr. Melvin L. Stone
(Radio Propagation Group)
**Inspector of Naval Material
495 Summer St.
Boston 10, Mass.

Westinghouse Electric Corp.
Defense Center-Baltimore
Tech. Info. Center
P.O. Box 1693
Baltimore 3, Md.
1 Attn: Mr. David Fales

RMS Engineering, Inc.
P.O. Box 6354, Station H
Atlanta 8, Ga.
1 Attn: Prof. William B. Wrigley
**Contract Administrator
Southeastern Area
Office of Naval Research
2110 G. St., N.W.
Washington 7, D.C.

Rand Corporation
1700 Main St.
Santa Monica, Calif
1 Attn: Dr. Cullen M. Crain
**Inspector of Naval Material
929 S. Broadway
Los Angeles 15, Calif.

~~W~~Pickard and Burns, Inc.
11103 Fourth Ave.
~~W~~Waltham 54, Mass.
() (Subsidiary of Gorham Corp)
111 Attn: Dr. J.C. Williams
**Inspector of Naval Material
495 Summer St.
Boston 10, Mass.

***Texas Technological College
Electrical Engineering Dept.
Lubbock, Texas
1 Attn: Prof. Harold Spuhler

111University of California
~~W~~Berkeley 4, Calif.
111 Attn: Dr. E. Pinney
**Office of Naval Research
Branch Office
1000 Geary St.
San Francisco 9, Calif.

~~W~~General Electric Corp.
~~W~~Court St.
~~W~~Syracuse, N.Y.
111 Attn: Dr. G.H. Millman

~~W~~Battelle Memorial Institute
~~W~~505 King Ave.
~~W~~Columbus 1. Ohio
111 Attn: Battelle Defender

~~W~~DASA Data Center
7735 State St.
~~W~~Santa Barbara, Calif.
111 Attn: Mgr., Warren W. Chan

*All requests for this report shall be
approved by the Office of Naval Research
(Code 418), OXford 6-4476.
**When document is classified, send a copy
of the receipt form to this addressee.
***Unclassified reports only.

~~W~~General Electric Co.
~~W~~Heavy Military Division
~~W~~Court Street Plant
~~W~~Syracuse, N.Y.
111 Attn: Dr. John Costas
Bldg. 9, Rom. 29

~~W~~Diamond Ordnance Fuze Laboratories
~~W~~Ordnance Corps
~~W~~Washington 25, D.C.
111 Attn: Mr. Pervy Griffen

TEPER 5 (3-63)